

# A Carrier-Based Two-Phase-Clamped DPWM Strategy With Zero-Sequence Voltage Injection for Three-Phase Quasi-Two-Stage Buck-Type Rectifiers

Junzhong Xu , Member, IEEE, Thiago Batista Soeiro , Senior Member, IEEE, Yang Wu , Student Member, IEEE, Fei Gao , Member, IEEE, Yong Wang , Member, IEEE, Houjun Tang, and Pavol Bauer , Senior Member, IEEE

**Abstract**—A three-phase buck-type rectifier features a step-down ac–dc conversion function, which is considered as a prominent solution for electric vehicle chargers and telecommunication systems integrated to the grid above 380 V line to line. However, traditional solutions for those applications employ cascaded architectures with an ac–dc boost-type stage and a dc–dc buck-type stage, which may suffer from high switching losses and large dc-link capacitor volume. To relieve this issue, a straightforward carrier-based two-phase-clamped discontinuous pulsewidth modulation (DPWM) strategy with generalized zero-sequence voltage injection is proposed in this article for the commonly employed cascaded circuit. This method can stop the switching actions in the front-end stage during two-third of the grid period, which can yield to the best switching loss reduction. The operations of the front- and back-end converter stages become highly coupled to each other, which reduces the size requirement of the capacitor in the dc link. Therefore, the equivalent circuit behaves as a quasi-two-stage buck-type rectifier allowing an enhancement of the system power density by improving power conversion efficiency and by reducing the volume of passive components and heat sink. The proposed carrier-based two-phase-clamped DPWM strategy is described, analyzed, validated, and compared with different pulsewidth modulation methods on PLECS-based simulation and a 5-kW prototype.

**Index Terms**—Buck-type rectifier, carrier-based, discontinuous pulsewidth modulation (DPWM), zero-sequence voltage injection.

## I. INTRODUCTION

THREE-PHASE buck-type rectifiers feature a step-down function widely employed in industrial applications, such

Manuscript received March 9, 2021; revised June 1, 2021, August 1, 2021, and September 27, 2021; accepted November 22, 2021. Date of publication November 25, 2021; date of current version January 19, 2022. This work was supported by the National Natural Science Foundation of China under Grant 51577118. Recommended for publication by Associate Editor D. Vinnikov. (Corresponding author: Yong Wang.)

Junzhong Xu, Fei Gao, Yong Wang, and Houjun Tang are with the Key Laboratory of Control of Power Transmission and Conversion, Ministry of Education, Shanghai Jiao Tong University, Shanghai 200240, China, and also with the Department of Electrical Engineering, Shanghai Jiao Tong University, Shanghai 200240, China (e-mail: junzhongxu@sjtu.edu.cn; fei.gao@sjtu.edu.cn; wangyong75@sjtu.edu.cn; hjtang@sjtu.edu.cn).

Thiago Batista Soeiro, Yang Wu, and Pavol Bauer are with the Department of Electrical Sustainable Energy, DC Systems, Energy Conversion and Storage Group, Delft University of Technology, 2628 CD Delft, The Netherlands (e-mail: t.batistasoeiro@tudelft.nl; y.wu-6@tudelft.nl; p.bauer@tudelft.nl).

Color versions of one or more figures in this article are available at <https://doi.org/10.1109/TPEL.2021.3130677>.

Digital Object Identifier 10.1109/TPEL.2021.3130677

as electric vehicle (EV) batteries charging systems, data centers, and power supplies for telecommunications, where the 480 or 380 V (line-to-line rms voltage) grid voltage can be stepped down to 250–450 V dc [1]–[4]. In practice, two-stage power converters are normally used to allow the power conversion from the three-phase ac grid to a dc bus with lower voltage, which consist of a front-end boost-type rectifier providing 650–800 V dc with a large capacitance in the dc link and a subsequent step-down dc–dc converter.

In order to achieve a smaller filter size and higher power efficiency for buck-type rectifiers, a wide variety of interesting solutions have been proposed on single-stage circuit topologies and their corresponding modulation strategies [5]–[15]. A three-phase six-switch buck-type power factor (PF) correction rectifier is studied in [5], and an ultrahigh efficiency can be achieved in comparison with other three-phase rectifier systems. The three-phase buck-type SWISS rectifier is introduced in [6] and [7], which can be a favorable solution for EV battery charger systems. A new modulation concept for the uni- and bidirectional SWISS rectifier is discussed in [8] to improve the current distortions at the grid voltage sector boundaries. To reduce the input current and voltage ripples of the traditional SWISS rectifier, an interleaved SWISS rectifier is presented in [9] and [12]. The delta-type current-source rectifier is designed in [10] to reduce the conduction loss in traditional current-source rectifiers [11], [13]. Although single-stage buck-type rectifiers are able to realize the voltage step-down directly, some technologies may suffer from a more complex modulation operating logic requiring overlap time between the semiconductor bridge because of the impressed output current [8], [9], [11], [16]. Several circuit technologies of single-stage buck-type rectifiers will display limited PF range [5]–[10]. Recently, with the promotion of commercial wide-bandgap semiconductor devices, i.e., silicon carbide (SiC), the losses for the conventional two-stage solution of such buck-type rectifier systems can be reduced significantly [17]–[19]. Therefore, a conventional two-stage rectifier circuit (cf. Fig. 1) turns to be favored in practice due to simpler modulation operating logic and wider PF range, where the front-end converter comprises a three-phase three-wire two-level six-switch voltage-source rectifier having inherent features such as low complexity and low cost, and the back-end circuit works as a dc–dc buck-type converter, as shown in Fig. 1.

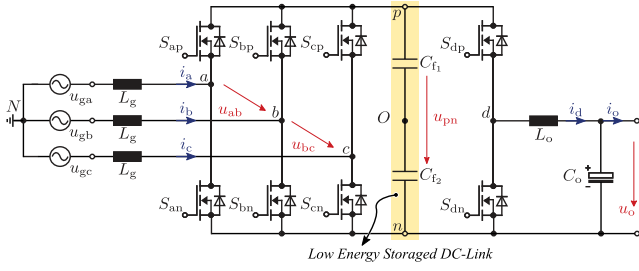


Fig. 1. Circuit topology for three-phase quasi-two-stage buck-type rectifier.

To further improve the power density, several advanced modulation strategies have been studied for the front-end circuit of Fig. 1, where two phases in the ac side are clamped, and no dc-link voltage control is needed, leading to a very small capacitance requirement in the dc link [20]–[28]. Such a circuit with low dc-link capacitance is called a three-phase quasi-two-stage buck-type rectifier in this article. One-phase modulation or two-phase-clamped discontinuous pulsewidth modulation (DPWM) has been previously investigated in [20]–[23] for motor drives or solar power generation systems, where only one phase leg out of three phase legs in the ac–dc power conversion stage performs the switching actions at the same time, and the converter with such a modulation can be called as electrolytic capacitorless pulsewidth modulation (PWM) converter. A comprehensive analysis in harmonic distortion and switching losses, and experimental validation of the two-phase-clamped DPWM has been performed for EV traction inverters in [24]. In [25], the two-phase-clamped DPWM has been applied in the fast dc-type EV charger, and a lookup table has been provided to implement such a modulation. Two-stage three-phase dc–ac buck-boost converters with synergetically controlled two-phase-clamped DPWM are well studied in [26], [27], in which a wider dc voltage can be achieved for the battery charger system. This converter functionality under regular and irregular grid conditions has been discussed in [28] as well. It is found that two-phase-clamped DPWM can yield to the best switching loss reduction in any known DPWM strategies for the front-end ac–dc circuit, i.e., the ones described in [17] and [29]–[32]. Other similar operations as the two-phase-clamped DPWM but with different topologies, e.g., Vienna-type front-end circuit [33], delta-switch-type front-end circuit [13], and series-resonant-type back-end circuit [34], have been proposed. However, for all previously studied two-phase-clamped DPWM strategies, the modulation operations for front- and back-end stages are independent, and the relationship with traditional modulation techniques (space-vector-based and carrier-based PWM techniques) is unclear. Additionally, the literature works lack a comprehensive performance comparison in both front- and back-end circuits among different PWM methods over the whole PF range, i.e.,  $PF = 1, \dots, -1$ .

To fill these gaps, a new straightforward carrier-based two-phase-clamped DPWM strategy with generalized zero-sequence voltage injection is proposed in this article, where the back-end dc–dc stage can be regarded as the fourth phase leg of the three-phase quasi-two-stage buck-type rectifier. Herein, the modulation signals are determined by the reference voltage and the zero-sequence voltage, and the equivalent relationship with the space vector implementation and the duty cycle expression

implementation is clarified. With such an approach, it is easy to carry out systematic analysis of performance characteristics about the modulator over the whole PF range in terms of switching losses, current ripples, and common-mode voltage (CMV) based on the universal theoretical model in [29], [32], and [35]. To the best of the authors' knowledge, there is no literature work that has developed such a straightforward carrier-based DPWM approach with generalized zero-sequence injection into the grid-connected rectifier applications with two-phase-clamped functionality.

This article contributes into the following points.

- 1) A carrier-based two-phase-clamped DPWM strategy with generalized zero-sequence voltage injection is proposed.
- 2) Theoretical basis of the proposed strategy and the relationship with different implementations are clarified.
- 3) Comprehensive analysis of different performance characteristics over the whole PF range for the two-phase-clamped DPWM strategy in both front- and back-end stages is given. This includes a detailed derivation and analysis of the semiconductor switching loss and filter current ripple functions (CRFs), and generated CMV, among others.
- 4) The benchmarking of different PWM strategies for the grid-connected quasi-two-stage buck-type rectifiers in theory, simulations, and experiments is performed.

The rest of this article is organized as follows. In Section II, the detailed principle of the studied carrier-based two-phase-clamped DPWM strategy with zero-sequence voltage injection is illustrated, and its relationship with other PWM implementations is clarified. In Section III, performance characteristics in terms of switching losses, current ripples, and CMV are investigated mathematically and compared with other classical PWM methods with constant dc-link voltage. In Section IV, the key parameters of the prototype are designed, and the studied carrier-based two-phase-clamped DPWM strategy is evaluated and benchmarked against other traditional PWM methods with constant dc-link voltage in both simulation and a 5-kW 400-V dc output prototype. Finally, Section V concludes this article.

## II. WORKING PRINCIPLE OF THE STUDIED TWO-PHASE-CLAMPED DPWM STRATEGY

The circuit topology for the studied three-phase quasi-two-stage buck-type rectifier is depicted in Fig. 1. As previously discussed, the front- and back-end circuits are connected to each other through a dc link with low energy storage capability, which makes the operation of both circuits highly coupled to each other. Herein, the front-end ac–dc stage is composed of six active switches,  $S_{abc,p/n}$ , and the back-end dc–dc stage is structured by another two active switches,  $S_{d,p/n}$ , which are connected with the front-end stage via the dc-link capacitors,  $C_{f1, f2}$ ;  $u_{pn}$  is the dc-link voltage;  $u_{gabc}$  and  $i_{abc}$  are the grid input voltage and current, respectively;  $L_g$  represents the ac phase inductor;  $i_d$  is the phase current for the back-end buck circuit;  $u_o$  and  $i_o$  are the output voltage and current of the system, respectively;  $L_o$  is the output inductor; and  $C_o$  is the output capacitor. To make the two-phase-clamped DPWM strategy valid over each fundamental period, two phases with maximum voltage magnitude should

always be clamped. Assuming no voltage drop across the circuit components and a symmetric ac voltage, the output voltage  $u_o$  of the studied three-phase quasi-two-stage buck-type rectifier should be adjusted to values starting from zero to

$$u_o \leq u_{pn,\min} = \frac{3}{2}U_m \quad (1)$$

where  $U_m$  is the magnitude of the grid phase voltage.

### A. Carrier-Based Two-Phase-Clamped DPWM Strategy With Zero-Sequence Voltage Injection

Assuming that the operating condition is balanced and symmetrical, the reference voltages ( $u_a^*$ ,  $u_b^*$ , and  $u_c^*$ ) for the front-end ac–dc stage can be expressed as

$$\begin{cases} u_a^* = U_m^* \cos \omega t \\ u_b^* = U_m^* \cos (\omega t - 2\pi/3) \\ u_c^* = U_m^* \cos (\omega t + 2\pi/3) \end{cases} \quad (2)$$

where  $\omega$  is the phase angle speed and  $U_m^*$  is the magnitude of the reference voltages. After that, the dc-link voltage can be decided by

$$u_{pn} = u_{pN} - u_{nN}. \quad (3)$$

It is noted that in the three-phase two-level ac–dc converter, only the phase leg with the maximum or minimum references can be clamped; otherwise, it will cause the problem of over-modulation in another phase and affect the waveform quality [36]. Therefore,  $u_{pN}$  and  $u_{nN}$  are uniquely determined, i.e.,  $u_{pN} = \max\{u_a^*, u_b^*, u_c^*\}$  and  $u_{nN} = \min\{u_a^*, u_b^*, u_c^*\}$ , and there is no need to control  $u_{pn}$  to get the desired shape.

Thereafter, the reference voltage for the back-end dc–dc stage with the reference output voltage,  $u_o^*$ , is defined as

$$u_d^* = u_o^* + u_{nN} = u_o^* + \min\{u_a^*, u_b^*, u_c^*\}. \quad (4)$$

The zero-sequence voltage of the modulation voltage of the studied method can be determined by

$$\begin{aligned} u_0 &= u_{NO}^* = u_{Nn}^* + u_{nO}^* = -\min\{u_a^*, u_b^*, u_c^*\} - \frac{1}{2}u_{pn} \\ &= -\frac{1}{2}(\max\{u_a^*, u_b^*, u_c^*\} + \min\{u_a^*, u_b^*, u_c^*\}) \\ &= \frac{1}{2}\text{mid}\{u_a^*, u_b^*, u_c^*\}. \end{aligned} \quad (5)$$

Finally, the modulation waveforms  $u_a^{**}$ ,  $u_b^{**}$ ,  $u_c^{**}$ , and  $u_d^*$  of the studied carrier-based two-phase-clamped DPWM strategy with zero-sequence voltage injection can be obtained to compare with the PWM triangular carriers

$$\begin{cases} u_a^{**} = u_a^* + u_0 = U_m^* \cos(\omega t) + u_0 \\ u_b^{**} = u_b^* + u_0 = U_m^* \cos(\omega t - 2\pi/3) + u_0 \\ u_c^{**} = u_c^* + u_0 = U_m^* \cos(\omega t + 2\pi/3) + u_0 \\ u_d^* = u_d^* + u_0 = u_o^* + \min\{u_a^*, u_b^*, u_c^*\} + u_0. \end{cases} \quad (6)$$

The block diagram of the implementation of the studied carrier-based PWM modulator and its simplified illustration are presented in Fig. 2. It is found that the modulation waveforms  $u_a^{**}$ ,  $u_b^{**}$ , and  $u_c^{**}$  of the two-phase-clamped DPWM strategy in

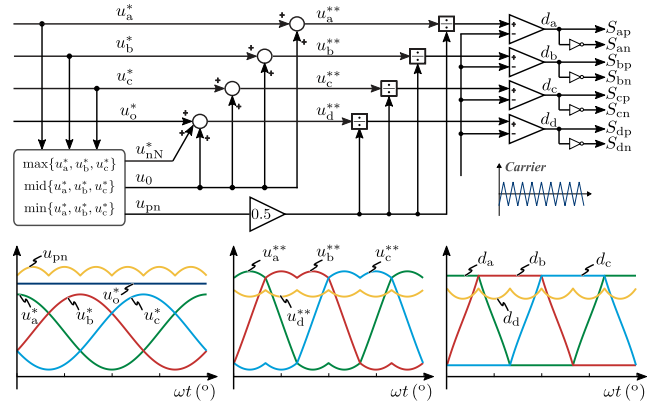


Fig. 2. Block diagram of the carrier-based PWM modulator and the simplified illustration of the studied PWM method.

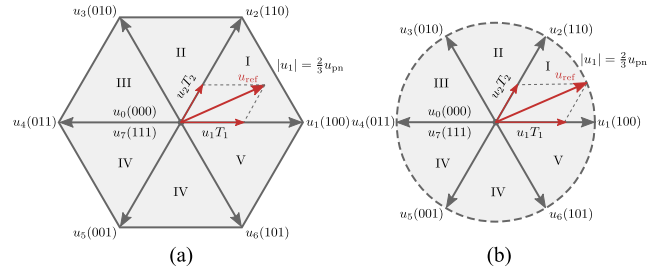


Fig. 3. Space vector diagram for the (a) traditional PWM methods and (b) studied two-phase-clamped DPWM.

the front-end stage are exactly the same as the ones for the conventional space vector pulsewidth modulation (SVPWM) [29]. With the injection of the zero-sequence voltage, the studied two-phase-clamped DPWM method can be similarly realized by the modern digital signal processing (DSP) with enhanced pulsewidth modulator units as other PWM methods, where the modulation signals are loaded to compare registers per phase directly and compared with inner counters to generate the switching signals,  $S_a$ ,  $S_b$ ,  $S_c$ , and  $S_d$ .

### B. Space-Vector Modulation Concept for the Studied Two-Phase-Clamped DPWM Strategy

In the traditional space vector modulation for two-stage ac–dc converters, the dc-link voltage is normally kept fixed or constant, and thus, the boundary of the space vector diagram is a hexagon, as shown in Fig. 3(a). To synthesize a sinusoidal ac voltage output, as an example in Sector I, the space vector  $u_{ref}$  of the sampled reference voltage is synthesized by using the two nearest active voltage vectors  $u_1$  (1 0 0) and  $u_2$  (1 1 0) and zero-voltage vector  $u_0$  (0 0 0) or  $u_7$  (1 1 1) in one switching period  $T_s$ . It is noted that the zero-voltage vector is indispensable to compensate the remaining time in one switching period. If both  $u_0$  (0 0 0) and  $u_7$  (1 1 1) are used, no phase leg can be clamped, and these modulations are known as continuous PWM, while, if either  $u_0$  (0 0 0) or  $u_7$  (1 1 1) are utilized, only one phase leg is clamped, which are called discontinuous PWM.

To realize the two-phase-clamped DPWM [20]–[23], as the example presented in Fig. 3(b), the execution time of the two nearest active voltage vectors  $u_1$  (1 0 0) and  $u_2$  (1 1 0), i.e.,  $T_1$

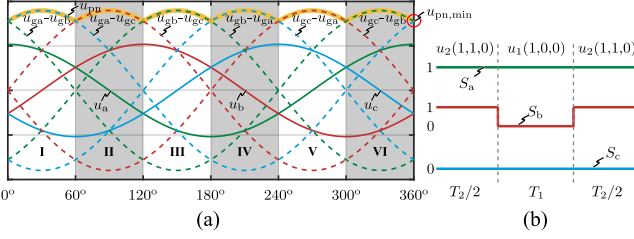


Fig. 4. Sectors definition and switching sequence for the two-phase-clamped DPWM. (a) Sectors' definition. (b) Switching sequence in Sector I.

and  $T_2$ , should satisfy the following equations:

$$\begin{cases} u_{\text{ref}} T_s = u_1 T_1 + u_2 T_2 \\ T_1 = \frac{\sqrt{3}|u_{\text{ref}}| (\sqrt{3} \cos \omega t + \sin \omega t)}{2u_{\text{pn}}} T_s \\ T_2 = \frac{\sqrt{3}|u_{\text{ref}}| \sin \omega t}{u_{\text{pn}}} T_s. \end{cases} \quad (7)$$

Since neither  $u_0$  (0 0 0) nor  $u_7$  (1 1 1) can be selected to construct the reference voltage,  $u_{\text{ref}}$ ,  $T_1 + T_2 = T_s$ , and the relationship between  $u_{\text{ref}}$  and  $u_{\text{pn}}$  can be derived as

$$u_{\text{pn}} = \left( \frac{3}{2} \cos \omega t + \frac{\sqrt{3}}{2} \sin \omega t \right) |u_{\text{ref}}|. \quad (8)$$

Therefore, with the variable dc-link voltage controlled by the back-end dc–dc circuit, a sinusoidal ac voltage output in the front-end ac–dc circuit can be obtained without any zero-voltage vector, i.e., two phase legs are clamped at any instant either high (positive dc rail) or low (negative dc rail).

### C. Relationship Between Space-Vector-Based and Carrier-Based PWM Implementation

Taking Sector I as an example, i.e.,  $0^\circ \leq \varphi \leq 60^\circ$  in Fig. 4(a), (8) can also be expressed as

$$u_{\text{pn}} = U_m^* \cos \omega t - U_m^* \cos(\omega t + 2\pi/3) = u_a^* - u_c^* \quad (9)$$

which is exactly the same as

$$u_{\text{pn}} = \max\{u_a^*, u_b^*, u_c^*\} - \min\{u_a^*, u_b^*, u_c^*\}. \quad (10)$$

Moreover, as seen in Fig. 4(b), phase  $b$  is the only phase that is kept switching, whose duty cycle  $d_b$  is

$$d_b = \frac{T_2}{T_s} = \frac{\sqrt{3}|u_{\text{ref}}| \sin \omega t}{u_{\text{pn}}}. \quad (11)$$

Then, the modulation wave for phase  $b$  with the triangular carrier wave can be calculated by

$$\begin{aligned} u_b^{**} &= \frac{1}{2} u_{\text{pn}} (2d_b - 1) = \left( \frac{3\sqrt{3}}{4} \sin \omega t - \frac{3}{2} \cos \omega t \right) |u_{\text{ref}}| \\ &= \frac{3}{2} U_m^* \cos(\omega t - 2\pi/3) = u_b^* + 0.5u_b^* = u_b^* + u_0. \end{aligned} \quad (12)$$

The result derived based on the space vector modulation concept is exactly the same as the one defined in (6). This conclusion as well as the same expression of  $u_{\text{pn}}$  obtained in Sector I can be generalized to the other sectors. Consequently,

these two different implementations of the two-phase-clamped DPWM strategy are inherently equivalent.

## III. ANALYTICAL COMPARISON OF PERFORMANCE CHARACTERISTICS

The analytical models of the modulator performance in terms of switching losses, current distortion, and CMV in the quasi-two-stage buck-type rectifier with the studied two-phase-clamped DPWM, the conventional SVPWM, and the DPWM methods summarized in [37] are discussed in this section. For the traditional SVPWM and DPWM, the dc-link voltage is considered constant, which is set as  $u_{\text{pn}} = \sqrt{3}U_m$ . To comprehensively evaluate the performance of the modulator, the PF angle,  $\varphi$ , range  $0^\circ \leq \varphi \leq 180^\circ$ , and the modulation index,  $M = u_o/U_m$ , range  $0 \leq M \leq 1.5$ , are used. Consider a sinusoidal ac current shape; a constant dc voltage; no voltage drop and losses across the filter inductors, i.e.,  $U_m^* \approx U_m$ ; and a switching frequency  $f_s$  being much larger than the grid frequency  $f_g$ , i.e.,  $f_s \gg f_g$ .

### A. Switching Loss Function (SLF)

For the theoretical calculation of the switching losses, each phase current ( $i_a$ ,  $i_b$ ,  $i_c$ , and  $i_d$ ) can be expressed as

$$\begin{cases} i_a = I_m \cos(\omega t - \varphi) \\ i_b = I_m \cos(\omega t - 2\pi/3 - \varphi) \\ i_c = I_m \cos(\omega t + 2\pi/3 - \varphi) \\ i_d = \frac{3U_m I_m}{2u_o} \cos \varphi = \frac{3I_m}{2M} \cos \varphi. \end{cases} \quad (13)$$

After that, the average switching power loss for the device in phase  $x$  ( $x \in \{a, b, c\}$ ) over a fundamental period can be defined as

$$P_{\text{sw}_x} = \frac{1}{2\pi U_b} f_s E_{\text{on,off,rr}} \int_0^{2\pi} u_{\text{pn}}(\omega t) I_x(\omega t) d\omega t \quad (14)$$

where  $E_{\text{on,off,rr}}$  represents a lumped switching losses per commutation for a specified dc voltage and output current,  $U_b$  is the datasheet reference voltage,  $f_s$  represents the constant switching frequency of the devices, and  $I_x(\omega t)$  equals zero in the intervals where no switching occurs and equals to the absolute value of the corresponding phase current  $|i_x(\omega t)|$  otherwise. Normalizing the total switching losses  $P_{\text{sw}}$  to  $P_0$ , the SLF of different modulators for the quasi-two-stage buck-type rectifier studied in this article can be found as

$$P_0 = \frac{2\sqrt{3}U_m I_m}{\pi U_b} f_s E_{\text{on,off,rr}} \quad (15)$$

$$\text{SLF}_{\text{ac}} = \frac{P_{\text{sw}_{a/b/c}}}{P_0} \quad (16)$$

$$\text{SLF}_{\text{dc}} = \frac{P_{\text{swd}}}{P_0}. \quad (17)$$

Applying (14) to (17), the SLF for the two-phase-clamped DPWM in the front-end ac–dc stage can be obtained as in (18). The SLF for continuous PWM methods is 1, and that for other PWM methods in the front-end with a constant dc-link voltage can be found in [29]–[32]. The SLF for the two-phase-clamped DPWM and other PWM methods with a constant dc-link voltage

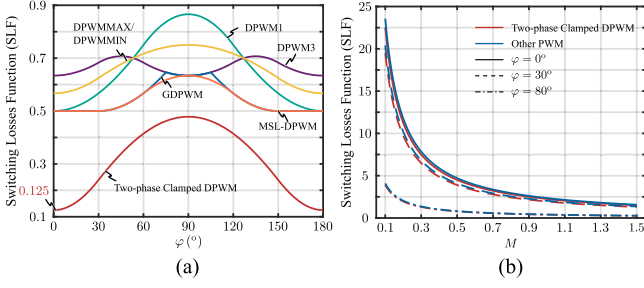


Fig. 5. SLF comparison for (a) front-end ac-dc stage and (b) back-end dc-dc stage.

in the back-end can be derived as in (19)

$$\text{SLF}_{\text{ac}} = \begin{cases} \frac{\cos \varphi}{8} + \frac{\varphi \sin \varphi}{2}, & 0 \leq \varphi < \frac{\pi}{6} \\ \frac{(2\pi + 3\sqrt{3}) \sin \varphi}{24}, & \frac{\pi}{6} \leq \varphi < \frac{5\pi}{6} \\ -\frac{\cos \varphi}{8} + \frac{(\pi - \varphi) \sin \varphi}{2}, & \frac{5\pi}{6} \leq \varphi \leq \pi \end{cases} \quad (18)$$

$$\text{SLF}_{\text{dc}} = \begin{cases} \frac{9}{4M} |\cos \varphi|, & \text{studied DPWM} \\ \frac{3\pi}{4M} |\cos \varphi|, & \text{other PWM.} \end{cases} \quad (19)$$

The comparisons of SLFs for different PWM methods in both the front- and back-end stages are shown in Fig. 5. The SLF in the front-end stage is dependent on the PF angle  $\varphi$ , while that in the back-end stage varies with the modulation index  $M$ . As seen in Fig. 5(a), the application of two-phase-clamped DPWM in the front-end stage can remarkably reduce the switching losses, i.e., it is able to reduce 75% of the losses found in the minimum switching loss DPWM (MSL-DPWM) in [30] at unity PF, which yields to the best switching loss reduction in any known DPWM strategies. Since the grid voltage and dc-link voltage are fixed, the SLF in the front-end stage is independent of  $M$ . In Fig. 5(b), the SLF of the two-phase-clamped DPWM is still lower than other PWM strategies with any  $M$  at the back-end dc-dc stage, because the average value of its dc-link voltage is smaller than that of the other strategies. With  $|\cos(\varphi)|$  reduced, the SLF in the back-end stage is decreased accordingly. As Fig. 5 indicates, the studied two-phase-clamped DPWM method can achieve the minimum switching losses over the whole  $\varphi$  and  $M$  range in the quasi-two-stage system, which will lead to a simplified thermal management with low cost, improved efficiency, and higher power density of the converter.

### B. Current Ripple Function

The winding and core losses of the filter inductor depend on the current ripple. Therefore, the output current ripple determined by the selected modulator gives an indication about the magnetic losses. To demonstrate the performance of the current ripple, the mathematical formulation can be derived from the terminal pulse voltage and current waveforms shown in Fig. 6, where phase  $a$  is selected to represent the current performance in the front-end stage. The time intervals  $t_1$ – $t_4$  can be obtained from the PWM period  $T_s$  and the modulation waveforms  $u_a^{**}$

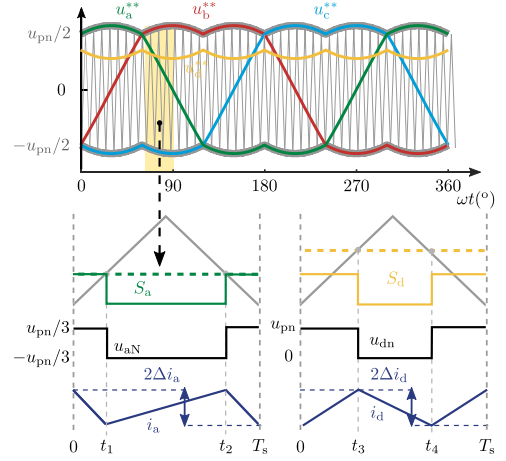


Fig. 6. Illustration of the switching sequence and current ripple of  $i_a$  and  $i_d$ .

and  $u_d^{**}$ . For example,  $t_1$  and  $t_3$  in Fig. 6 are

$$t_1 = \frac{2u_a^{**}/u_{\text{pn}} + 1}{4} T_s \quad (20)$$

$$t_3 = \frac{2u_d^{**}/u_{\text{pn}} + 1}{4} T_s. \quad (21)$$

Then, the squared rms value of the current ripple of  $i_a$  and  $i_d$  can be expressed as

$$\Delta I_{a,\text{rms}}^2 = \frac{1}{2\pi} \int_0^{2\pi} \left( \frac{1}{T_s} \int_0^{T_s} \Delta i_a^2 d\tau \right) d\omega t \quad (22)$$

$$\Delta I_{d,\text{rms}}^2 = \frac{1}{2\pi} \int_0^{2\pi} \left( \frac{1}{T_s} \int_0^{T_s} \Delta i_d^2 d\tau \right) d\omega t \quad (23)$$

where the deviations of  $\Delta i_b$  and  $\Delta i_d$  are

$$\Delta i_a = i_b - i_{b,\text{avg}} = \frac{1}{L_g} \int (u_{ga} - u_{aN}) dt \quad (24)$$

$$\Delta i_d = i_d - i_{d,\text{avg}} = \frac{1}{L_o} \int (u_{dn} - u_o) dt. \quad (25)$$

By normalizing the squared rms value of the current ripple  $\Delta I_{a,\text{rms}}^2$  and  $\Delta I_{d,\text{rms}}^2$  to  $\Delta I_0^2$  in (26)

$$\Delta I_0^2 = \frac{T_s^2 U_{\text{dc}}^2}{2\pi L^2} \quad (26)$$

the CRF for  $i_a$  and  $i_d$  can be calculated as

$$\text{CRF}_{i_a} = \sqrt{\frac{\Delta I_{a,\text{rms}}^2}{\Delta I_0^2}} \quad (27)$$

$$\text{CRF}_{i_d} = \sqrt{\frac{\Delta I_{d,\text{rms}}^2}{\Delta I_0^2}}. \quad (28)$$

The comparisons of CRFs for different PWM methods in both front- and back-end stages are shown in Fig. 7. The CRF in the front-end stage is independent of  $\varphi$  and  $M$ , because the modulation index in the front-end stage, from  $u_{\text{abc}}^*$  to  $u_{\text{pn}}$ , is fixed, while that in the back-end stage varies with modulation index,  $M$ . As seen in Fig. 7(a), the application of two-phase-clamped DPWM in the front-end stage has the best current ripple performance as well in any known PWM strategies. In Fig. 7(b),

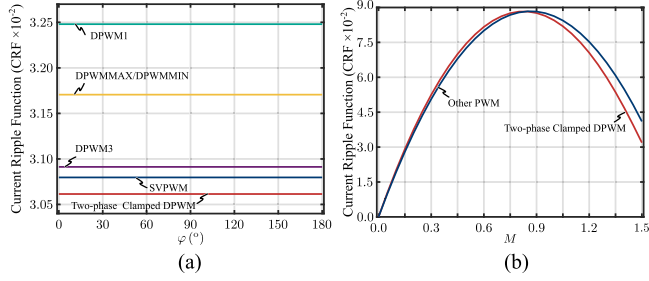


Fig. 7. CRF comparison at varied  $M$  for (a) front-end ac-dc stage and (b) back-end dc-dc stage.

the CRF of the two-phase-clamped DPWM is still higher than that in other PWM strategies at low  $M$ , but turns to be smaller at high  $M$ .

### C. Common-Mode Voltage

The CMV of the quasi-two-stage system is generally defined as the potential difference from the grid star point to the negative terminal of the output voltage ( $u_{Nn}$  in Fig. 1) as follows:

$$u_{cmv} = u_{NO} + \frac{u_{pn}}{2} = \frac{u_{ao} + u_{bo} + u_{co}}{3} + \frac{u_{pn}}{2}. \quad (29)$$

As discussed in Section II-B, since there is no zero-voltage vector used in the two-phase-clamped DPWM, the peak value of  $u_{NO}$  can be reduced from  $\pm u_{pn}/2$  to  $\pm u_{pn}/6$  in every switching period  $T_s$ , which yields the same effect as the reduced-CMV PWM methods studied in [17].

To further theoretically analyze the spectrum of the CMV, the double Fourier integral analysis is introduced. In general terms, the harmonic component of the phase-leg output voltage  $C_{mn}$  under given carrier index variable  $m$  (of the carrier frequency  $f_c$ ) and fundamental index variable  $n$  (of the modulating frequency  $f_o$ ) is given as

$$C_{mn} = \frac{1}{2\pi^2} \sum_{i=1}^6 \int_{y_s(i)}^{y_e(i)} \int_{x_r(i)}^{x_f(i)} u_{pn}(y) e^{j(m\omega_c x + n\omega_o y)} dx dy. \quad (30)$$

Assuming that  $u_{pn}$  only has dc and sixth-fundamental-frequency component, the high-frequency harmonic components of  $u_{cmv}$  can be expressed as

$$u_{cmv} = \sum_{m=1}^{\infty} \sum_{n=-\infty}^{\infty} C_{mn} \times \cos(m\omega_c t + n\omega_o t) \quad n = 3p, p = 0, 1, 2, \dots \quad (31)$$

where  $y_s(i)$ ,  $y_e(i)$ ,  $x_r(i)$ , and  $x_f(i)$  are the outer and inner double Fourier integral limits, which are listed in Table I.  $\omega_c = 2\pi f_c$  is the carrier angular frequency, and  $\omega_o = 2\pi f_o$  is the fundamental angular frequency.

Following the aforementioned calculations, the normalized CMV harmonics (to  $U_m$ ) of different PWM methods within the first carrier frequency, i.e.,  $m = 1$ , are shown in Fig. 8. Only the triple-harmonic components of the fundamental exist in the CMV harmonics. It can be found that the maximum CMV harmonic of the two-phase-clamped DPWM method is the lowest among the different methods. Since the resonant

TABLE I  
INTEGRATION LIMITS FOR DOUBLE FOURIER INTEGRAL

Sector	$y_s(i)$	$y_e(i)$	$x_r(i)$	$x_f(i)$
I	0	$\frac{\pi}{3}$	$-\pi$	$\pi$
II	$\frac{\pi}{3}$	$\frac{2\pi}{3}$	$-\frac{\pi(\sin \omega t + \sqrt{3} \cos \omega t)}{2 \sin \omega t}$	$\frac{\pi(\sin \omega t + \sqrt{3} \cos \omega t)}{2 \sin \omega t}$
III	$\frac{2\pi}{3}$	$\pi$	0	0
IV	$\pi$	$\frac{4\pi}{3}$	0	0
V	$\frac{4\pi}{3}$	$\frac{5\pi}{3}$	$-\frac{\pi(\sin \omega t - \sqrt{3} \cos \omega t)}{2 \sin \omega t}$	$\frac{\pi(\sin \omega t - \sqrt{3} \cos \omega t)}{2 \sin \omega t}$
VI	$\frac{5\pi}{3}$	$2\pi$	$-\pi$	$\pi$

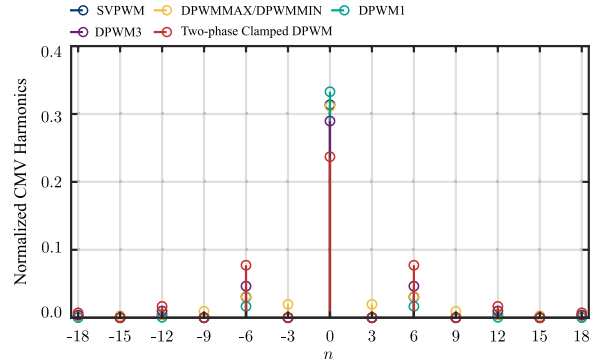


Fig. 8. Normalized CMV harmonics within the first carrier frequency.

TABLE II  
SPECIFICATIONS OF THE EVALUATED THREE-PHASE QUASI-TWO-STAGE BUCK-TYPE RECTIFIER

Variables	Parameters	Value
$P_o$	Rated power	5 kW
$U_m$	Grid voltage	311 V
$\omega$	Grid angular frequency	$2\pi \times 50$ rad/s
$f_s$	switching frequency	36 kHz

frequency of the common-mode circuit is close to its carrier frequency for grid-connection applications [38], the studied two-phase-clamped DPWM will bring about a lower ground leakage current in practice as well.

## IV. SIMULATION AND EXPERIMENTAL RESULTS

To validate the effectiveness of the studied carrier-based two-phase-clamped DPWM strategy, simulations and experimental tests are conducted and compared with different PWM methods on the three-phase quasi-two-stage buck-type rectifier. First, a PLECS-based simulation is carried out. Thereafter, the studied DPWM method is operated on a digital-control hardware platform with the DSP from Texas Instruments, TMS320F28379D. In both the simulation and the experiment, SiC MOSFETs from CREE C3M0120090J [39] are used. The main specifications for the three-phase quasi-two-stage buck-type rectifier are listed in Table II.

The studied topology circuit of the three-phase quasi-two-stage buck-type rectifier and its corresponding control blocks implemented in this section are shown in Fig. 9. Herein, the back-end circuit is operated as a three-channel PWM interleaved dc-dc buck converter. This feature will enhance the loss distribution among the semiconductors or better current shared between the

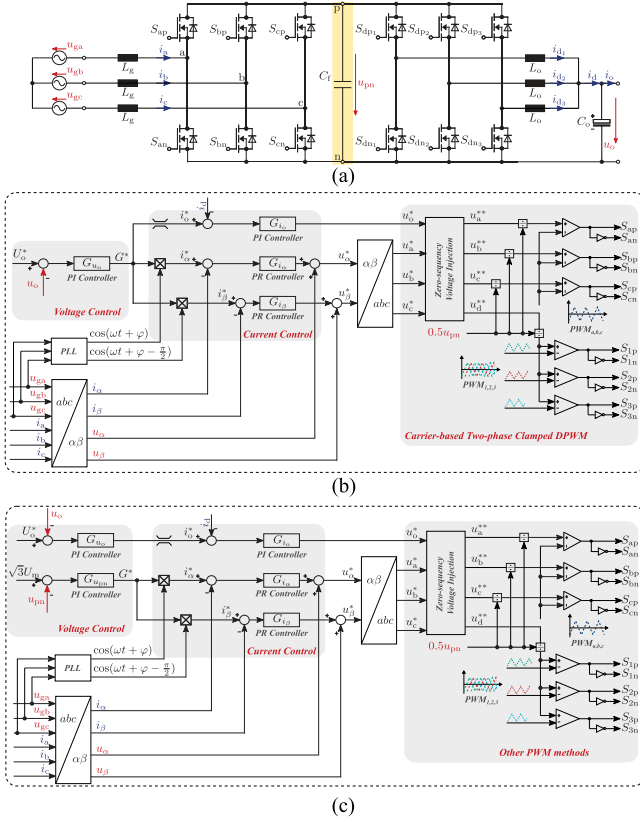


Fig. 9. Overall control block diagram of the three-phase quasi-two-stage buck-type rectifier, (a) circuit topology, (b) with two-phase clamping DPWM strategy, and (c) with other PWM strategies.

parallel circuits than the hard paralleling of semiconductors, and it will cancel out the high-frequency harmonics in both output voltage and current. It is noted that to keep a constant dc-link voltage for other PWM methods, a larger dc-link capacitor and an additional dc-link voltage controller are needed, as shown in Fig. 9(c). Since DPWMMAX and DPWMMIN methods have the same performance in switching losses, current distortion, and CMV, only the DPWMMAX method is studied in this section.

### A. Key Parameter Design

The current ripple flowing through  $L_o$  is defined as

$$\Delta i_{L_o,pp} = \frac{u_{pn} - u_o}{L_o f_s} \frac{u_o}{u_{pn}} = \frac{u_o}{L_o f_s} \left(1 - \frac{u_o}{u_{pn}}\right) \quad (32)$$

$$\Delta i_{L_o,pp,max} = \frac{u_o}{L_o f_s} \left(1 - \frac{u_o}{u_{pn,max}}\right) \quad (33)$$

$$\Delta i_{o,pp,max} = \frac{\Delta i_{L_o,pp,max}}{N} \quad (34)$$

where  $N$  is the number of paralleled interleaved buck converters and  $\Delta i_{L_o,pp,max}$  is the maximum current ripple across  $L_o$ . Therefore, the inductance value of  $L_o$  can then be selected according to

$$L_o \geq \frac{u_o}{\Delta i_{L_o,pp,max} f_s} \left(1 - \frac{u_o}{u_{pn,max}}\right). \quad (35)$$

Similarly, taking phase  $a$  as an example, the current ripple across  $L_g$  is given by

$$\Delta i_{L_g,pp} = \frac{u_{aN} - u_{ga}}{L_g f_s} \quad (36)$$

$$\Delta i_{L_g,pp,max} = \Delta i_{L_g,pp} \Big|_{u_{ga}=0} = \frac{u_{pn,max}}{6L_g f_s}. \quad (37)$$

Accordingly, the inductance value of  $L_g$  can then be selected as

$$L_g \geq \frac{u_{pn,max}}{6\Delta i_{L_g,pp,max} f_s}. \quad (38)$$

It is noted that herein, the filter inductor designs are based on the maximum current ripple requirement [40], and the proposed expressions are similar to all studied PWM methods, and the main difference is found in the reference value of  $u_{pn,max}$ . If the harmonic distortion for grid compliance is considered for a high-order filter at the ac side, e.g.,  $LCL$  filter, the local rms current ripple method can be calculated [41], and the impact of the PWM methods on the converter-side inductor design can be referenced to Fig. 7, where the two-phase-clamped DPWM strategy requires the minimum filter demand.

The maximum peak-to-peak high-frequency voltage ripple across the output capacitor  $C_o$ ,  $\Delta u_{C_o,pp,max}$ , occurs when the output current ripple is the maximum, which is determined by

$$\Delta u_{C_o,pp,max} = \frac{1}{2Nf_s} \cdot \frac{1}{2} \Delta i_{o,pp,max} = \frac{\Delta i_{L_o,pp,max}}{8C_o f_s N^2}. \quad (39)$$

Thereafter, the output capacitor  $C_o$  can be decided as

$$C_o \geq \frac{\Delta i_{L_o,pp,max}}{8f_s N^2 \Delta u_{C_o,pp,max}}. \quad (40)$$

The worst peak-to-peak voltage ripple across the dc-link capacitor  $C_f$ ,  $\Delta u_{C_f,pp,max}$ , occurs when assuming that there is no current passing through the back-end stage

$$\Delta u_{C_f,pp} = \frac{P_o}{u_{pn}} \frac{1}{f_s C_f} \left(1 - \frac{u_o}{u_{pn}}\right) \quad (41)$$

$$\Delta u_{C_f,pp,max} = \frac{P_o}{f_s C_f} \left(\frac{1}{u_{pn,max}} - \frac{u_o}{u_{pn,max}^2}\right). \quad (42)$$

Hence, the dc-link capacitor  $C_f$  can be obtained as

$$C_f \geq \frac{P_o}{f_s \Delta u_{C_f,pp,max}} \left(\frac{1}{u_{pn,max}} - \frac{u_o}{u_{pn,max}^2}\right). \quad (43)$$

In particular, for the two-phase-clamped DPWM strategy, the resonant frequency of the  $L_o$ - $C_f$  filter should be ten times higher than the frequency of the six-pulse shaped dc-link voltage, i.e.,  $6f_g$ , to avoid an additional resonance suppressing control [42]. Under such a condition,  $C_f$  has an upper bound

$$\frac{1}{2\pi\sqrt{L_o C_f}} \geq 10 \cdot 6f_g \quad (44)$$

$$C_f \leq \frac{1}{14400L_o f_g^2}. \quad (45)$$

Different PWM strategies impact less on  $C_o$  because their requirements of  $\Delta u_{C_o,pp,max}$  are the same. However, the two-phase-clamped DPWM strategy allows a larger  $\Delta u_{C_f,pp,max}$  in

TABLE III  
VALUE OF FILTER INDUCTORS AND CAPACITORS FOR THE THREE-PHASE  
QUASI-TWO-STAGE BUCK-TYPE RECTIFIER

Variables	Parameters	Value
$L_g$	Grid inductor	720 $\mu\text{H}$
$L_o$	Output inductor	450 $\mu\text{H}$
$C_o$	Output capacitor	280 $\mu\text{F}$
$C_f$	DC-link capacitor (with studied PWM)	5 $\mu\text{F}$
$C_f$	DC-link capacitor (with other PWM)	360 $\mu\text{F}$

the dc link, while the other PWM strategies must have very low  $\Delta u_{C_f,pp,max}$  to keep the ac current sinusoidal. Consequently, the resulting dc-link capacitance value in  $C_f$  for the two-phase-clamped DPWM strategy will be much smaller.

The design constraints of (35), (38), (40), (43), and (45) define a design space within the filter inductance or capacitance must be selected. In this section, setting

$$\Delta i_{L_g,pp,max} \leq 2 \cdot \frac{P_o}{NU_o} \quad (46)$$

$$\Delta i_{L_g,pp,max} \leq 40\% \cdot \frac{2P_o}{3U_m} \quad (47)$$

$$\Delta u_{C_o,pp,max} \leq 5\% \cdot U_o \quad (48)$$

$$\Delta u_{C_f,pp,max} \leq \begin{cases} 20\% \cdot U_m, & \text{studied DPWM} \\ 0.1\% \cdot U_m, & \text{other PWM} \end{cases} \quad (49)$$

the filter inductance and the capacitance with enough margin are given in Table III. Herein, larger  $C_o$  and  $C_f$  for the other conventional PWM methods are selected to make sure that a constant output and dc-link voltage can be obtained. A simple design guideline is provided in this section that was used to assemble the prototype, to evaluate the effectiveness of the proposed carrier-based two-phase-clamped DPWM strategy, and finally to benchmark all the studied PWM methods. If the three-phase quasi-two-stage buck-type rectifier is applied for industrial applications, specific standards are required to be met, which may lead to a different passive filtering design.

### B. Simulation Results

Figs. 10 and 11 show the simulation waveforms of the dc-link voltage  $u_{pn}$ , output current  $i_o$ , ac voltages  $u_{gabc}$ , three phase currents  $i_{abc}$ , modulation waveforms  $u_{abcd}^{**}$ , and duty cycles  $d_{abcd}$  with  $\varphi$  increased from  $0^\circ$  at  $t = 0.02$  s to  $180^\circ$  at  $t = 0.32$  s, and also with output voltage  $u_o$  increased from 200 V at  $t = 0.02$  s to 450 V at  $t = 0.32$  s, respectively, when using the studied two-phase-clamped DPWM strategy. To keep the power constant at 5 kVA, a dc voltage source is used and the magnitude value of the grid current  $I_m$  is controlled to be 10.71 A. It is evident that the implemented carrier-based two-phase-clamped DPWM can adapt well with wide range of  $\varphi$  and  $u_o$ , according to the analytical development in (2)–(6).

Fig. 12 compares the simulation results of  $i_a$  and  $i_{d1}$  with various PWM methods at  $\varphi = 0^\circ$  and  $P = 5$  W. Since the back-end stage operates as a three-channel PWM interleaved dc–dc converter, the current ripple cannot be truly reflected in

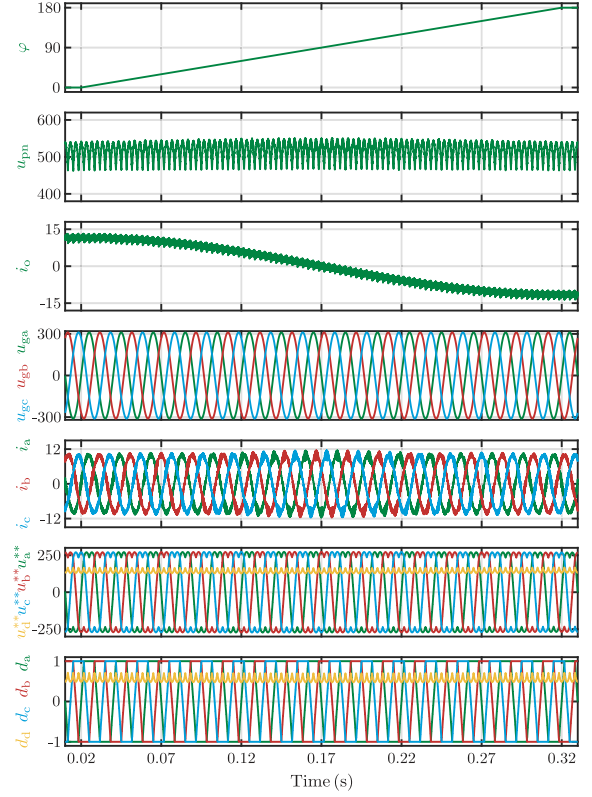


Fig. 10. Simulation waveforms of the dc-link voltage  $u_{pn}$ , output current  $i_o$ , ac voltages  $u_{gabc}$ , ac currents  $i_{abc}$ , modulation waveforms  $u_{abcd}^{**}$ , and three phase duty cycles  $d_{abcd}$  with  $\varphi$  increased from  $0^\circ$  at  $t = 0.02$  s to  $180^\circ$  at  $t = 0.32$  s, when using the two-phase-clamped DPWM method.

the measured total output current  $i_d$ . Consequently, the current in a single output inductor  $L_o$ , i.e.,  $i_{d1}$ , is plotted in Fig. 12(b) to represent  $i_d$ . By visual inspection, one can observe that the current ripple of  $i_a$  obtained with the two-phase-clamped DPWM can be slightly lower than any of that obtained with other PWM methods. The current ripple of  $i_d$  with the studied DPWM strategy is not constant because the dc-link voltage  $u_{pn}$  is fluctuating, while the ripple with the SVPWM method is constant, which is the same as in other DPWM methods.

To obtain a better insight and to validate the results of the theoretical analysis, the switching losses and the current total harmonic distortion (THD) of  $i_a$  in the front-end ac–dc stage for various PWM methods with different  $\varphi$  are compared in Fig. 13, while keeping  $I_m = 10.71$  A. The datasheet values of  $E_{on}$  and  $E_{off}$  are used and built into the thermal model of the SiC MOSFET in the PLECS simulation. As expected, the switching loss performance of the studied two-phase-clamped DPWM is the lowest than any other PWM methods, which can reduced nearly 87.5% switching losses compared to the SVPWM at the unity PF. Moreover, the current THD of  $i_a$  does not change significantly with  $\varphi$ , and that of the studied two-phase-clamped DPWM is the best as well, which matches the analysis in Section III-B. It is noted that due to the fact that only an  $L$  filter is used at the ac side, and all harmonic components are considered, the current THD observed in simulation is relatively high. The comparison of switching losses and harmonic current of the back-end stage for different PWM methods with different

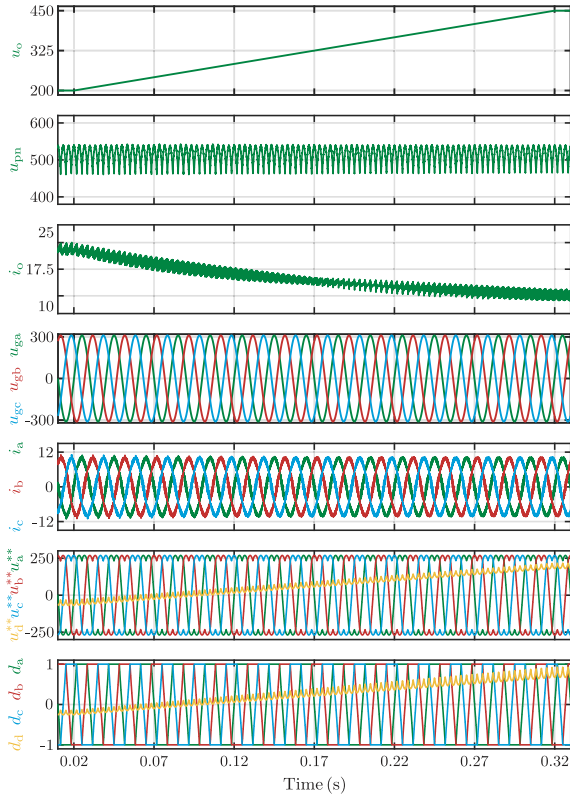


Fig. 11. Simulation waveforms of the dc-link voltage  $u_{pn}$ , output current  $i_o$ , ac voltages  $u_{gabc}$ , ac currents  $i_{abc}$ , modulation waveforms  $u_{abcd}^{**}$ , and duty cycles  $d_{abcd}$  with the output voltage  $u_o$  increased from 200 V at  $t = 0.02$  s to 450 V at  $t = 0.32$  s, when using the two-phase-clamped DPWM method.

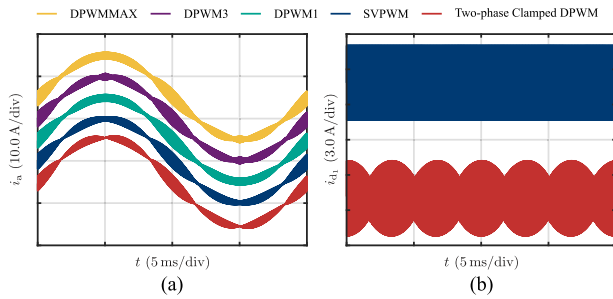


Fig. 12. Comparison of the ac and dc current in simulation among various PWM methods at  $\varphi = 0^\circ$  and  $u_o = 400$  V. (a)  $i_a$ . (b)  $i_{d1}$ .

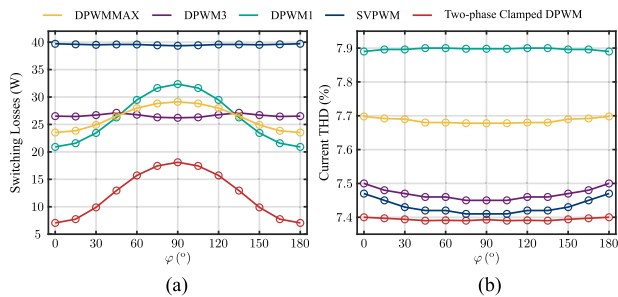


Fig. 13. Switching losses and current THD comparison at varied  $\varphi$  in simulation for the front-end ac-dc stage. (a) Switching losses. (b) Current THD. Note that due to the fact that only  $L$  filter is used at the ac side, and all harmonic components are considered in the analysis, the current THD observed in simulation is relatively high.

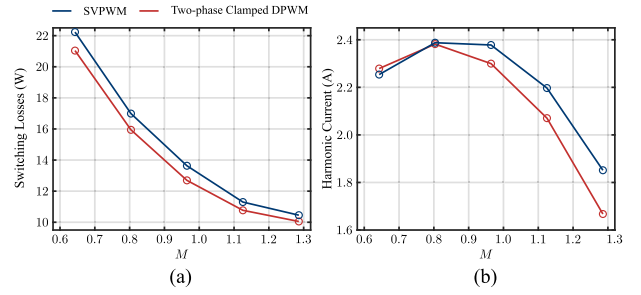


Fig. 14. Switching losses and harmonic current comparison at varied  $M$  in simulation for the back-end dc-dc stage. (a) Switching losses. (b) Harmonic current.

TABLE IV  
COMPARISON OF CMV HARMONICS WITHIN THE FIRST CARRIER FREQUENCY DETERMINED BY ANALYTICAL CALCULATIONS AND SIMULATIONS WITH THE TWO-PHASE CLAMPED DPWM

n	Calculation	Simulation	Deviation (%)
-18	0.0071	0.0071	-0.4346
-12	0.0167	0.0166	-0.3393
-6	0.0772	0.0768	-0.5331
0	0.2371	0.2371	0.0060
6	0.0772	0.0776	0.4903
12	0.0167	0.0167	0.4859
18	0.0071	0.0071	0.1573

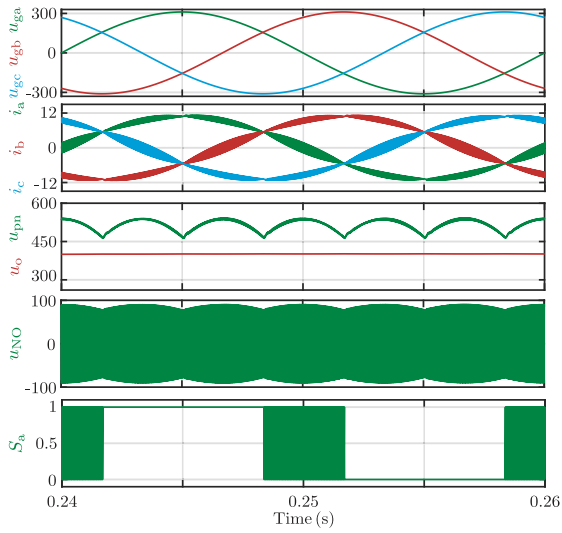
$M$  are given in Fig. 14. Herein, only SVPWM is performed to represent all the PWM methods with constant dc-link voltage, and the harmonic current  $I_h$  is defined as [35]

$$I_h = \sqrt{I_{rms}^2 - I_{avg}^2} \quad (50)$$

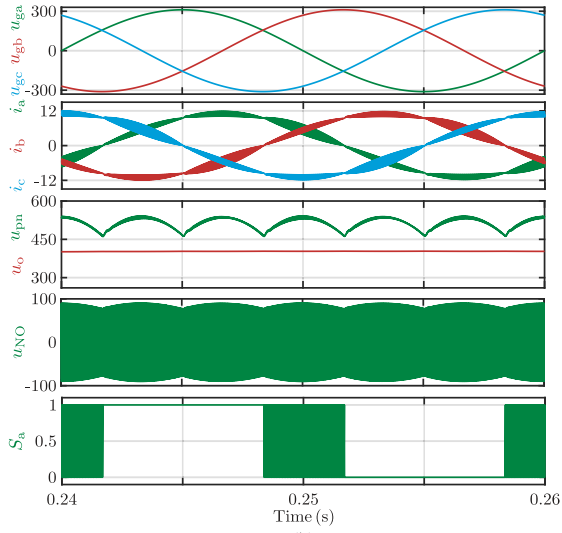
where  $I_{avg}$  and  $I_{rms}$  are the average and rms value of  $i_d$ . It can be found that the simulation results match well with the theoretical model in Figs. 5(b) and 7(b). The values of the CMV harmonics within the first carrier frequency calculated with the theoretical modeling are compared to the results obtained with the simulation, as listed in Table IV. It shows good accuracy of the CMV modeling built in Section III-C. Therefore, the effectiveness of the SLF, CRF, and CMV models in Section III has been proved.

Fig. 15 shows the simulation results of the steady-state operation of the three-phase quasi-two-stage buck-type rectifier with the two-phase-clamped DPWM strategy at  $u_o = 400$  V and  $I_m = 10.71$  A. Three specific cases are selected in Fig. 15. The first one is the unity PF rectifier mode with resistive load, where  $\varphi = 0^\circ$ ; the second one is the rectifier mode as well where  $\varphi = 30^\circ$ ; and the last one is the STATCOM mode, where  $\varphi = 90^\circ$  without dc resistive load. It can be seen that in all cases, the carrier-based two-phase-clamped DPWM strategy works well with different operating modes. Two-third of the switching signal is clamped, while sinusoidal input ac currents are obtained. The peak value of  $u_{NO}$  is  $\pm u_{pn}/6$  featuring the characteristic of suppressing CMV.

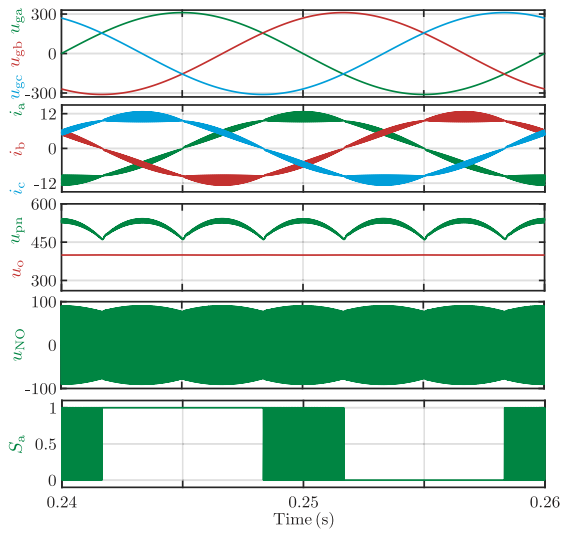
Fig. 16 shows the simulation results of the transient responses of the three-phase quasi-two-stage buck-type rectifier



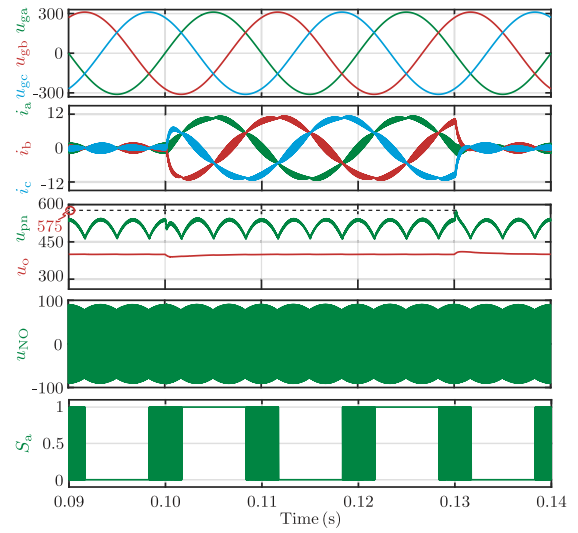
(a)



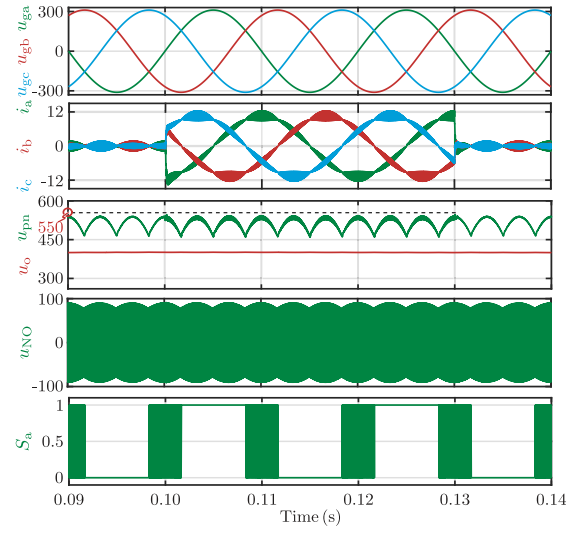
(b)



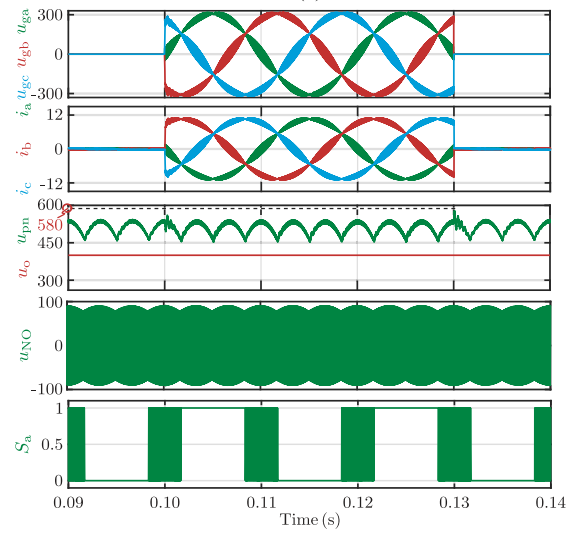
(c)



(a)



(b)



(c)

Fig. 15. Simulation results of the two-phase-clamped DPWM with different operation modes. (a)  $\varphi = 0^\circ$  unity PF rectifier mode. (b)  $\varphi = 30^\circ$  rectifier mode. (c)  $\varphi = 90^\circ$  STATCOM mode.

Fig. 16. Simulation results of the transient responses with the two-phase-clamped DPWM when dc-side load/current reference step changed from no-load to full-load and full-load to no-load. (a)  $\varphi = 0^\circ$  unity PF rectifier mode. (b)  $\varphi = 90^\circ$  STATCOM mode. (c)  $\varphi = 180^\circ$  inverter mode.

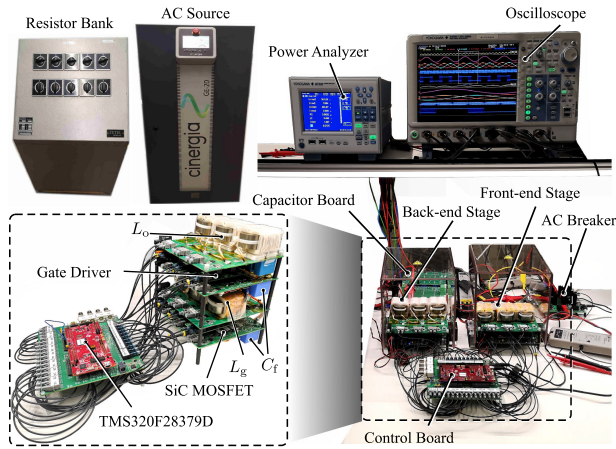


Fig. 17. Schematic diagram of the experimental setup.

with the two-phase-clamped DPWM when load/current reference changed from no load to full load at  $t = 0.1$  s and full load to no load at  $t = 0.13$  s. In all cases, i.e., the unity PF rectifier, STATCOM, and inverter modes, the two-phase-clamped DPWM method performs well during the dynamics, where the switching signal is clamped at two-third of fundamental period as expected. It can be seen that in Fig. 16, there exists a voltage overshoot or undershoot at the load transient period. Since the capacitance for the quasi-two-stage structure is much lower than that for the conventional two-stage design, the voltage increment or decrement in the dc-link capacitor will be larger, which is about 8% higher than the maximum operating value. However, such voltage overshoot or undershoot can be confined within the safe operating area of the semiconductor devices that have to block this voltage. Additionally, the variations in the dc link during transient can be relieved by slowing down the response time of the dynamic by reducing the bandwidth of the controllers.

### C. Experimental Results

A 5-kW prototype based on the power electronic circuit presented in Fig. 9(a) is built to further validate the feasibility and superiority of the proposed carrier-based two-phase-clamped DPWM method. In experiments, the three-phase quasi-two-stage buck-type rectifier is operated in inverter, rectifier, and STATCOM modes working with different PWM methods. The experimental setup and the detailed photos for the constructed three-phase quasi-two-stage buck-type rectifier are shown in Fig. 17. The average dc voltage in all experimental cases is controlled at 400 V. All of the experimental waveforms are recorded by the oscilloscope YOKOGAYA DLM4058, and the current THD and power conversion efficiency of the converter are tested by the power analyzer YOKOGAYA WT500.

Fig. 18 shows the experimental results for the three-phase quasi-two-stage buck-type rectifier at the steady state with the carrier-based zero-sequence voltage injection two-phase-clamped PWM method in different operating modes. Fig. 18(a) and (b) shows the experimental results at the rectifier mode. In this case, an ac voltage source with  $220 V_{\text{rms}}/50$  Hz is used, and a dc resistor bank is connected at the output port, where  $\varphi$  is set as  $0^\circ$  and  $30^\circ$ , respectively. Fig. 18(c) shows the experimental

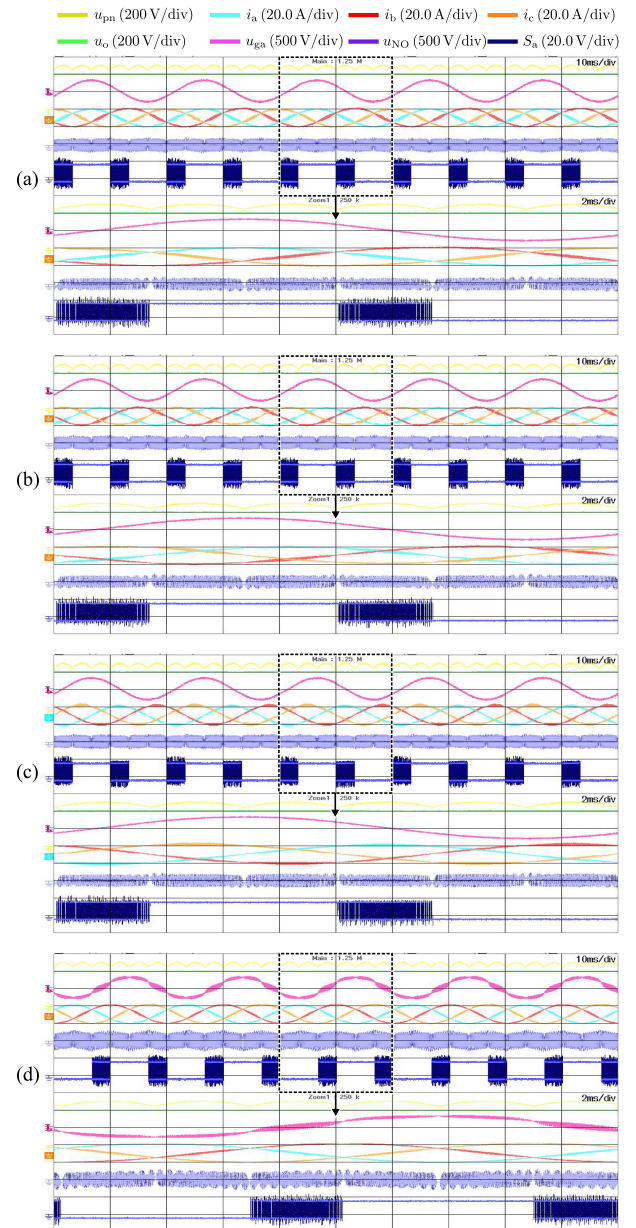


Fig. 18. Experimental results showing the steady states of the two-phase-clamped DPWM at (a)  $\varphi = 0^\circ$  unity PF rectifier mode, (b)  $\varphi = 30^\circ$  rectifier mode, (c)  $\varphi = 90^\circ$  STATCOM mode, and (d)  $\varphi = 180^\circ$  inverter mode. Note that the zoom function of the oscilloscope is used to show the details of the highlighted section of the experimental waveforms.

result at the STATCOM mode. In this case, an ac voltage source with  $220 V_{\text{rms}}/50$  Hz is used and no load is connected to the dc link, where  $\varphi$  is set to be  $90^\circ$ . Fig. 18(d) shows the experimental result at the inverter mode. In this case, a dc source with 400-V output is used, where  $\varphi$  is set at  $180^\circ$ . The experimental results demonstrate that the front-end ac currents  $i_a$ ,  $i_b$ , and  $i_c$  can effectively follow the sinusoidal shape of the input ac voltages, while the dc-link voltage is variable, attesting the feasibility of the studied circuit and control method depicted in Fig. 9(b). It is clearly observed that in Fig. 18, at every moment, two-third of the cycle of  $S_a$  is clamped, either at high (positive dc rail) or low (negative dc rail), where no switching actions occurs. Additionally, at the unity PF rectifier mode,  $S_a$  is switched only

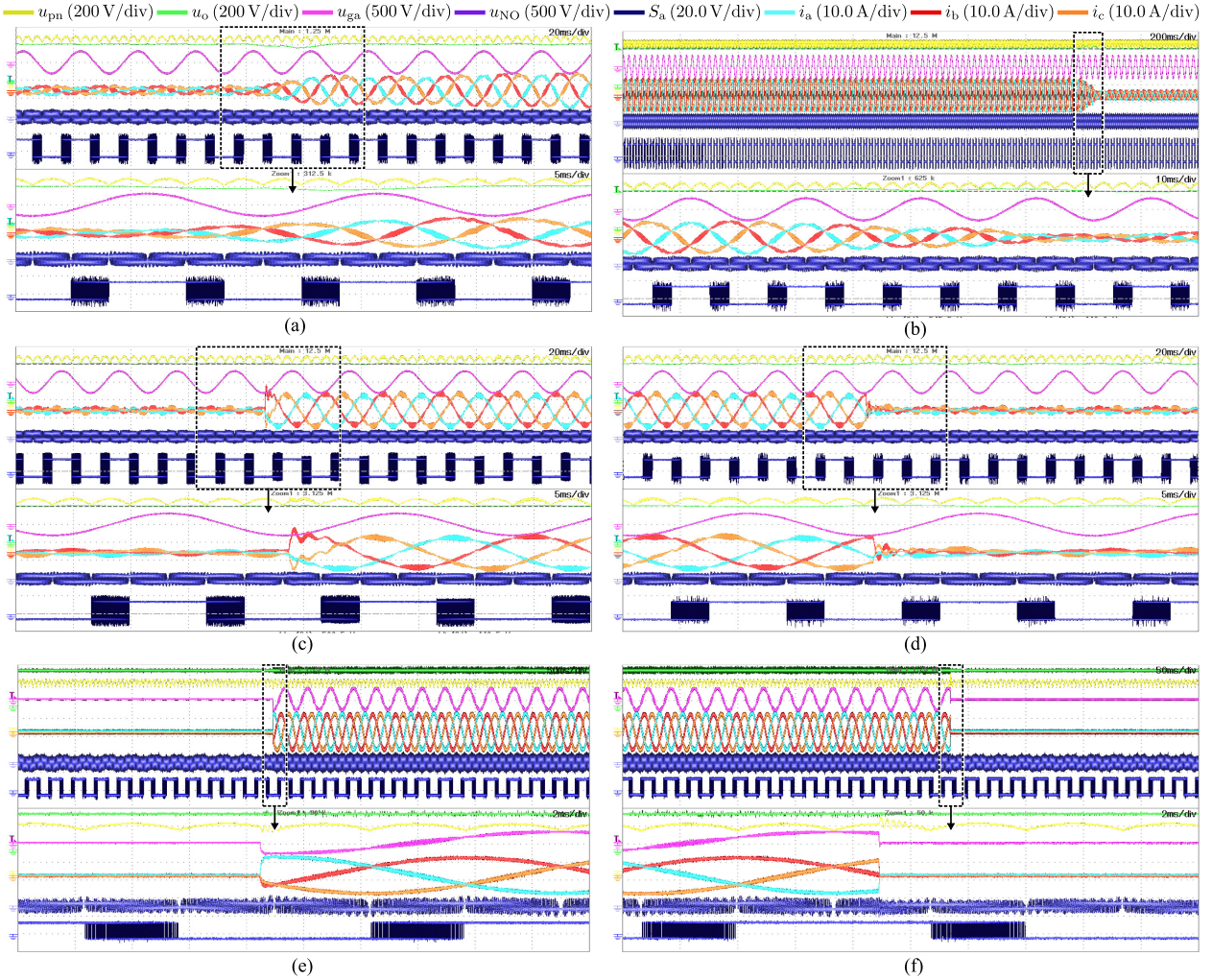


Fig. 19. Experimental results showing the transient states with two-phase-clamped DPWM at (a)  $\varphi = 0^\circ$  unity PF rectifier mode with load step changed from 30% to 80% full load, (b)  $\varphi = 0^\circ$  unity PF rectifier mode with load step changed from 80% to 30% full load, (c)  $\varphi = 90^\circ$  STATCOM mode with current reference step change from 1 to 9 A, (d)  $\varphi = 90^\circ$  STATCOM mode with current reference step change from 9 to 1 A, (e)  $\varphi = 180^\circ$  inverter mode with load step changed from full load to no load, and (f)  $\varphi = 180^\circ$  inverter mode with load step changed from full load to no load. Note that the zoom function of the oscilloscope is used to show the details of the highlighted section of the experimental waveforms.

at the lowest current magnitude, which can reduce the switching losses of the front-end stage considerably. All of the experimental cases show that the proposed straightforward carrier-based two-phase-clamped PWM method with zero-sequence voltage injection can adapt to the changes of the set phase angle  $\varphi$  and operating modes, which match well with the steady-state simulation results shown in Fig. 15.

Fig. 19 shows the transient-state experimental results for the three-phase quasi-two-stage buck-type rectifier with the proposed carrier-based two-phase-clamped DPWM method. Fig. 19(a) and (b) shows the experimental results at  $\varphi = 0^\circ$  unity PF rectifier mode with load step-up from 30% to 80% full load and step-down from 80% to 30% full load. It is noted that in this case, the dc-load change is achieved by switching four switches together on the resistor bank, which is difficult to achieve a full synchronization of the value change, so that the dynamic transition time shown in experiments is not as short as that in the simulation. Fig. 19(c) and (d) shows the experimental results at  $\varphi = 90^\circ$  STATCOM mode with current reference step-up from 1 to 9 A, and step-down from 9 to 1 A, nearly 9%–85%

full load (reactive). Fig. 19(e) and (f) shows the experimental results at  $\varphi = 180^\circ$  inverter mode with load step-up from no load to full load, and step-down from full load to no load, which is controlled by the switching ON/OFF the ac breaker. In all cases, the proposed carrier-based two-phase-clamped DPWM method can still clamp the switching signal at two-third of the fundamental period, which meets the corresponding simulation results presented in Fig. 16. In Fig. 19(a) and (b), since the reaction time of the manual load change is long, there is no noticeable inductor current overshoot/undershoot, as well as the dc capacitor voltage overshoot/undershoot at the transient instant. In Fig. 19(c) and (d), since the current reference is set via the communication, the current response is rapid. Additionally, the load-step change in Fig. 19(c) and (d) is nearly 9%–85% full load (reactive), and thus, inductor current distortion and the dc capacitor voltage overshoot/undershoot at the transient instant are more visible, but well within the safe operating area of the utilized semiconductor. In Fig. 19(e) and (f), it can be found that there is a nearly 50-V voltage overshoot in the dc link at the load step-down transient, which matches the simulations in

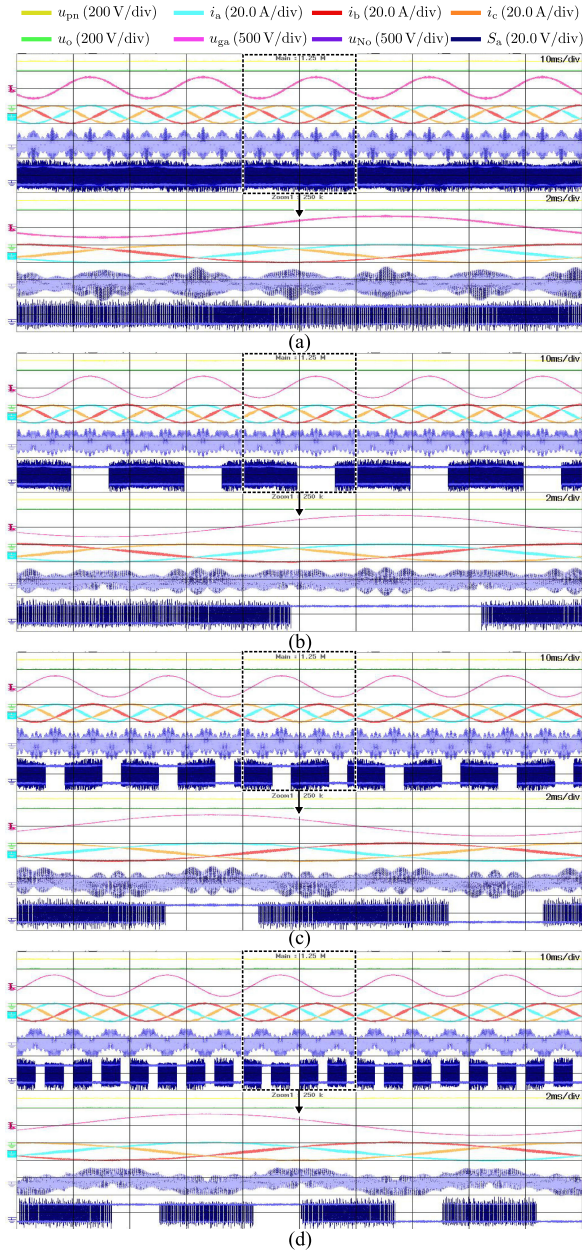


Fig. 20. Experimental results showing the steady states of other PWM methods with constant dc-link voltage in the rectifier mode at  $\varphi = 0^\circ$ : (a) with SVPWM, (b) with DPWMMAX, (c) with DPWM1, and (d) with DPWM3. Note that the zoom function of the oscilloscope is used to show the details of the highlighted section of the experimental waveforms.

Fig. 16(c), and the overvoltage of 50 V is within safe values because the MOSFETs used are 900 V rated. Due to the lower dc-link capacitance in the dc link, the voltage increment or decrement capacitor will be larger than that of the conventional two-stage design at the transient instant. The voltage overshoot/undershoot in the dc-link capacitor also deteriorates the performance of the current control loop and makes the inductor current distorted during transients.

Experimental results of the steady-state operation with other PWM methods following the control strategy depicted in Fig. 9(c) in the rectifier mode at  $\varphi = 0^\circ$  are shown in Fig. 20. The three-phase circuit works as a true two-stage power conversion

TABLE V  
COMPARISON OF THE MEASURED EXPERIMENTAL RESULTS

Mode	$\varphi$	PWM	THD	$\Delta P$	Efficiency
Rectifier	$0^\circ$	SVPWM	2.62 %	115.5 W	97.56 %
		DPWMMAX	2.03 %	105.3 W	97.78 %
		DPWM1	3.40 %	104.2 W	97.79 %
		DPWM3	2.44 %	105.2 W	97.78 %
		Studied	2.55 %	<b>77.7 W</b>	<b>98.38 %</b>
	$30^\circ$	SVPWM	2.33 %	108.9 W	97.22 %
		DPWMMAX	2.06 %	97.5 W	97.50 %
		DPWM1	3.41 %	99.3 W	97.46 %
		DPWM3	2.46 %	98.0 W	97.49 %
		Studied	2.52 %	<b>72.6 W</b>	<b>98.16 %</b>
STATCOM	$90^\circ$	SVPWM	1.38 %	94.4 W	-
		DPWMMAX	1.71 %	83.6 W	-
		DPWM1	1.58 %	83.8 W	-
		DPWM3	1.67 %	84.2 W	-
		Studied	1.69 %	<b>63.2 W</b>	-
Inverter	$180^\circ$	SVPWM	1.28 %	111.9 W	97.74 %
		DPWMMAX	1.42 %	102.1 W	97.95 %
		DPWM1	1.45 %	100.9 W	97.96 %
		DPWM3	1.34 %	102.6 W	97.94 %
		Studied	1.27 %	<b>69.1 W</b>	<b>98.61 %</b>

system working at  $P = 5$  kW with  $220V_{\text{rms}}/50$  Hz ac source and  $32\text{-}\Omega$  dc resistive load. The output voltage can also be controlled at 400 V, and the dc-link voltage is controlled constantly at 540 V with the other PWM methods, while effectively tracking the sinusoidal current reference. It can be seen that the clamped duration time of  $S_a$  for different DPWM methods in Fig. 20 is much shorter than that for the two-phased clamped DPWM method, i.e., only one-third of the cycle of  $S_a$ .

The essential part of the CMV,  $u_{\text{NO}}$ , is also measured in the experiments, as seen in Figs. 18 and 20. It can be found that the peak-to-peak value of  $u_{\text{NO}}$  with the two-phased clamped DPWM method is smaller than that of the others. To further study the CMV performance, CMV harmonic components of different PWM methods within the first carrier frequency are shown in Fig. 21. The result is calculated by the MATLAB 2020a with the data collected from the oscilloscope. The experimental results measured at the inverter mode are used. As can be seen, the maximum harmonic component of the two-phased clamped DPWM is the lowest, as predicted in the theoretical analysis.

Table V presents the current THD, power losses, and the efficiency of the two-converter-stage three-phase rectifier working with SVPWM, DPWMMAX, DPWM1, DPWM3, and the studied quasi-two-stage rectifier operating with two-phase-clamped DPWM for different  $\varphi$ . The load is changed at different  $\varphi$  to make the magnitude value of the grid current  $I_m$  constant at 10.71 A. The total power losses  $\Delta P = P_{\text{in}} - P_{\text{out}}$ , current THD, and the power efficiency (from 220 V<sub>ac</sub> to 400 V<sub>dc</sub>) are measured by the power analyzer YOKOGAWA WT500. The difference between the real power flowing into the converter and the one flowing out of the converter can be regarded as an estimation of the total losses in the converter, including the switching devices, passive components, and printed circuit board/cable connections. For the STATCOM mode, the output active power is zero, and thus, the measured input active power represents the circuit losses. As shown in Table V, with the

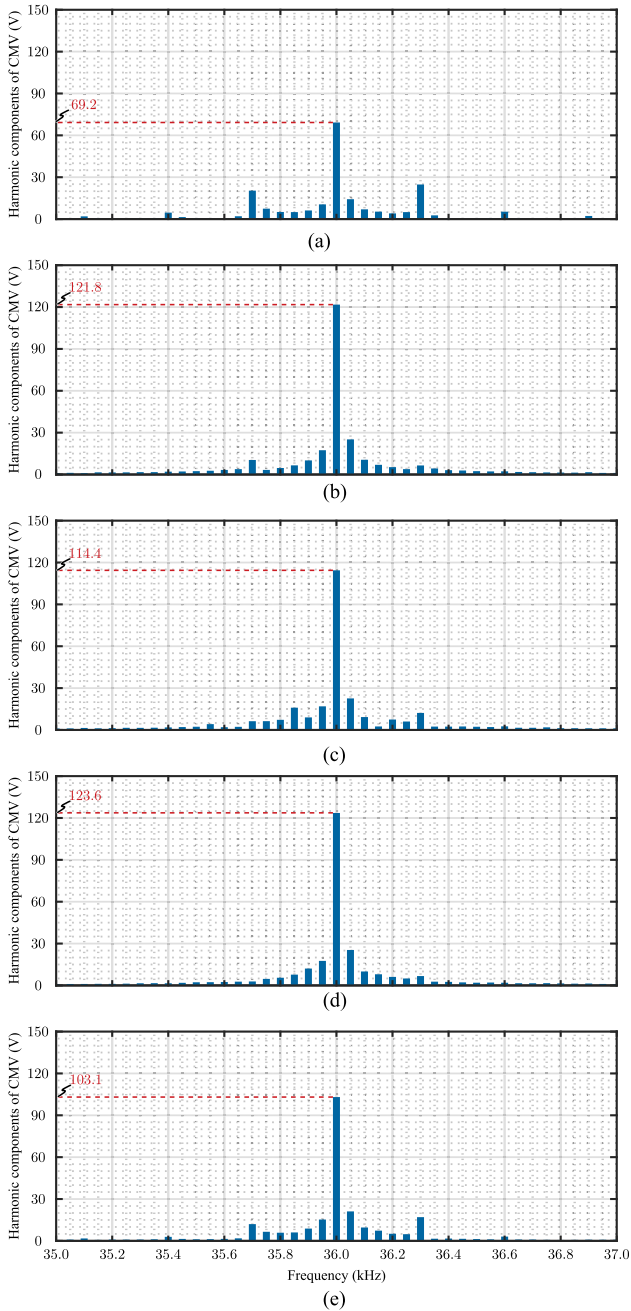


Fig. 21. Harmonic components of CMV: (a) with two-phase-clamped DPWM, (b) with SVPWM, (c) with DPWMMAX, (d) with DPWM1, and (e) with DPWM3.

two-phase-clamped DPWM, the power efficiency and power losses of the converter can be improved remarkably compared to the commonly employed PWM methods with constant dc-link voltage. The current THD of the two-phase-clamped DPWM is close to that of the SVPWM. Since only the harmonics components below the 50th order are considered in the power analyzer, the measured current THD results are lower than the ones obtained from the simulation results in Fig. 13(b). Moreover, the role of the voltage and current controllers have a much greater impact on current THD than the PWM strategy in experiments. Different PWM methods resulting in different low-frequency harmonics will influence the performance of the controllers.

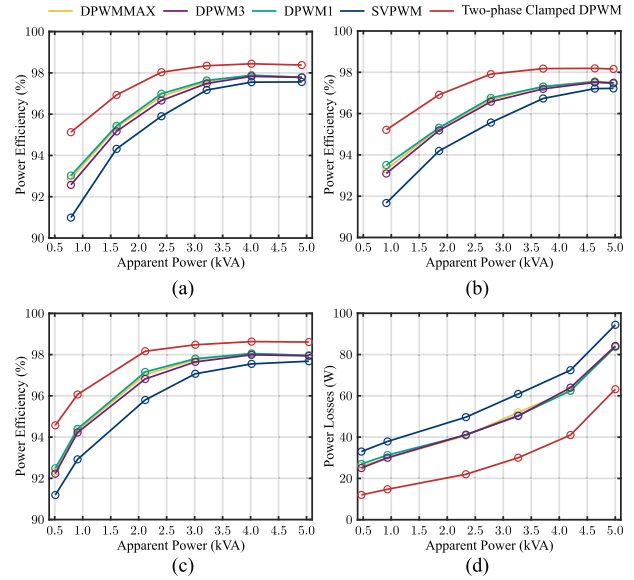


Fig. 22. Power efficiency and power losses comparison at different operating modes. (a)  $\varphi = 0^\circ$  unity PF rectifier mode. (b)  $\varphi = 30^\circ$  rectifier mode. (c)  $\varphi = 180^\circ$  inverter mode. (d)  $\varphi = 90^\circ$  STATCOM mode.

This effect is hard to be detected in the simulation, because the sampling delay and other nonideal factors that influence the control bandwidth do not exist in the simulation. Therefore, the effect of the PWM method on current ripple cannot be well presented in the measured current THD results.

Fig. 22 shows the power efficiency and power losses comparison among different PWM methods at different operating modes. In the STATCOM mode, the measured input active power is regarded as an estimation of the total losses in the converter, as presented in Fig. 22(d). It can be seen that, with traditional DPWM methods, the power efficiency and losses of the converter can be improved relative to the SVPWM method, and with the two-phase-clamped DPWM, the advantage can be further increased leading to the highest efficiency or the lowest power losses in the three-phase quasi-two-stage buck-type rectifier. All in all, the presented experimental cases have shown that a remarkable reduction on power losses and CMV with the two-phase-clamped DPWM method is possible in the three-phase quasi-two-stage buck-type rectifier. This confirms the superiority of this modulation method when compared with other traditional PWM strategies with constant dc-link voltage. Therefore, the validity and advantages of this DPWM strategy implemented with the proposed straightforward carrier-based zero-sequence voltage injection method are verified.

## V. CONCLUSION

This article has proposed a straightforward carrier-based two-phase-clamped DPWM strategy with generalized zero-sequence voltage injection for the three-phase quasi-two-stage buck-type rectifiers. The modulation waveforms of the proposed DPWM strategy in the front-end stage are exactly the same as the ones of the conventional SVPWM method, but the dc-link voltage is variable, which allows a low energy storage between the two cascaded converters. The principle of the two-phase-clamped

DPWM strategy from both carrier-based PWM and space vector concepts have been explained in detail. The mathematical models have been built and shown that the presented strategy has the best switching losses, current distortion, and CMV performance over other suitable PWM methods within all PF angle ranges. Both simulations and experimental results have been used to verify the effectiveness of the studied modulation method, and to prove the correctness of the presented theoretical analysis. It is found that in the experiments, the highest power efficiency or the lowest power losses can be obtained by the studied PWM method in comparison with other modulation methods, and the performance of CMV can also be improved.

## REFERENCES

- [1] J. W. Kolar and T. Friedli, "The essence of three-phase PFC rectifier systems—Part I," *IEEE Trans. Power Electron.*, vol. 28, no. 1, pp. 176–198, Feb. 2014.
- [2] A. Kuperman, U. Levy, J. Goren, A. Zafransky, and A. Savernin, "Battery charger for electric vehicle traction battery switch station," *IEEE Trans. Ind. Electron.*, vol. 60, no. 12, pp. 5391–5399, Dec. 2013.
- [3] G. Allée and W. Tschudi, "Edison redux: 380 Vdc brings reliability and efficiency to sustainable data centers," *IEEE Power Energy Mag.*, vol. 10, no. 6, pp. 50–59, Nov./Dec. 2012.
- [4] L. Wang, Z. Qin, T. Slangen, P. Bauer, and T. van Wijk, "Grid impact of electric vehicle fast charging stations: Trends, standards, issues and mitigation measures—An overview," *IEEE Open J. Power Electron.*, vol. 2, pp. 56–74, Jan. 2021. [Online]. Available: <https://ieeexplore.ieee.org/document/9336258>
- [5] A. Stupar, T. Friedli, J. Minibock, and J. W. Kolar, "Towards a 99% efficient three-phase buck-type PFC rectifier for 400-V DC distribution systems," *IEEE Trans. Power Electron.*, vol. 27, no. 4, pp. 1732–1744, Apr. 2012.
- [6] T. B. Soeiro, T. Friedli, and J. W. Kolar, "Swiss rectifier—A novel three-phase buck-type PFC topology for electric vehicle battery charging," in *Proc. 27th Annu. IEEE Appl. Power Electron. Conf. Expo.*, 2012, pp. 2617–2624.
- [7] T. B. Soeiro, T. Friedli, and J. W. Kolar, "Design and implementation of a three-phase buck-type third harmonic current injection PFC rectifier SR," *IEEE Trans. Power Electron.*, vol. 28, no. 4, pp. 1608–1621, Apr. 2013.
- [8] L. Schrittwieser, J. W. Kolar, and T. B. Soeiro, "Novel SWISS rectifier modulation scheme preventing input current distortions at sector boundaries," *IEEE Trans. Power Electron.*, vol. 32, no. 7, pp. 5771–5785, Jul. 2017.
- [9] L. Schrittwieser, M. Leibl, M. Haider, F. Thny, J. W. Kolar, and T. B. Soeiro, "99.3% efficient three-phase buck-type all-SiC SWISS rectifier for DC distribution systems," *IEEE Trans. Power Electron.*, vol. 34, no. 1, pp. 126–140, Jan. 2019.
- [10] B. Guo, F. Wang, and E. Aeloiza, "A novel three-phase current source rectifier with delta-type input connection to reduce the device conduction loss," *IEEE Trans. Power Electron.*, vol. 31, no. 2, pp. 1074–1084, Feb. 2016.
- [11] B. Guo, F. Wang, R. Burgos, and E. Aeloiza, "Modulation scheme analysis for high-efficiency three-phase buck-type rectifier considering different device combinations," *IEEE Trans. Power Electron.*, vol. 30, no. 9, pp. 4750–4761, Sep. 2015.
- [12] T. B. Soeiro, M. L. Heldwein, and J. W. Kolar, "Three-phase modular multilevel current source rectifiers for electric vehicle battery charging systems," in *Proc. Brazilian Power Electron. Conf.*, 2013, pp. 623–629.
- [13] T. B. Soeiro and P. Bauer, "Three-phase unidirectional quasi-single-stage delta-switch rectifier dc-dc buck converter," in *Proc. 45th Annu. Conf. IEEE Ind. Electron. Soc.*, 2019, pp. 3479–3484.
- [14] T. B. Soeiro, G. J. M. de Sousa, M. S. Ortmann, and M. L. Heldwein, "Three-phase unidirectional buck-type third harmonic injection rectifier concepts," in *Proc. IEEE Appl. Power Electron. Conf. Expo.*, 2014, pp. 928–934.
- [15] T. B. Soeiro, G. J. Maia, M. S. Ortmann, and M. L. Heldwein, "High efficiency three-phase unidirectional bucktype PFC rectifier concepts," in *Proc. 39th Annu. Conf. IEEE Ind. Electron. Soc.*, 2013, pp. 7763–7768.
- [16] L. K. Ries, T. B. Soeiro, M. S. Ortmann, and M. L. Heldwein, "Analysis of carrier-based pwm patterns for a three-phase five-level bidirectional buck boost-type rectifier," *IEEE Trans. Power Electron.*, vol. 32, no. 8, pp. 6005–6017, Aug. 2017.
- [17] J. Xu, J. Han, Y. Wang, M. Ali, and H. Tang, "High-frequency SiC three-phase VSIs with common-mode voltage reduction and improved performance using novel tri-state PWM method," *IEEE Trans. Power Electron.*, vol. 34, no. 2, pp. 1809–1822, Feb. 2019.
- [18] N. Oswald, P. Anthony, N. McNeill, and B. H. Stark, "An experimental investigation of the tradeoff between switching losses and EMI generation with hard-switched all-Si, Si-SiC, and all-SiC device combinations," *IEEE Trans. Power Electron.*, vol. 29, no. 5, pp. 2393–2407, May 2014.
- [19] Z. Zhang, F. Wang, L. M. Tolbert, B. J. Blalock, and D. J. Costinett, "Evaluation of switching performance of SiC devices in PWM inverter-fed induction motor drives," *IEEE Trans. Power Electron.*, vol. 30, no. 10, pp. 5701–5711, Oct. 2015.
- [20] Q. Lei and F. Z. Peng, "Space vector pulsewidth amplitude modulation for a buck-boost voltage/current source inverter," *IEEE Trans. Power Electron.*, vol. 29, no. 1, pp. 266–274, Jan. 2014.
- [21] K. Park, "One-phase modulation without DC link control for three-phase rectifier with LCL filter," in *Proc. 10th Int. Conf. Power Electron. ECCE Asia*, 2019, pp. 1–6.
- [22] H. Fujita, "Switching loss analysis of a three-phase solar power conditioner using a single-phase PWM control method," in *Proc. IEEE Energy Convers. Congr. Expo.*, 2010, pp. 618–623.
- [23] H. Shin, J. Ha, and W. Lee, "Active power control for minimum switching of three-phase electrolytic capacitor-less PWM converter," in *Proc. IEEE Energy Convers. Congr. Expo.*, 2013, pp. 783–788.
- [24] D. Wu, H. Qamar, H. Qamar, and R. Ayyanar, "Comprehensive analysis and experimental validation of 240°-clamped space vector PWM technique eliminating zero states for EV traction inverters with dynamic DC link," *IEEE Trans. Power Electron.*, vol. 35, no. 12, pp. 13295–13307, Dec. 2020.
- [25] T. B. Soeiro and P. Bauer, "Fast DC-type electric vehicle charger based on a quasi-direct boost-buck rectifier," in *Proc. AEIT Int. Conf. Elect. Electron. Technol. Automot.*, 2019, pp. 1–6.
- [26] D. Menzi, D. Bortis, and J. W. Kolar, "Three-phase two-phase-clamped boost-buck unity power factor rectifier employing novel variable dc link voltage input current control," in *Proc. IEEE Int. Power Electron. Appl. Conf. Expo.*, 2018, pp. 1–8.
- [27] M. Antivachis, J. A. Anderson, D. Bortis, and J. W. Kolar, "Analysis of a synergetically controlled two-stage three-phase DC/AC buck-boost converter," *CPSS Trans. Power Electron. Appl.*, vol. 5, no. 1, pp. 34–53, 2020.
- [28] D. B. Y. Li, J. Azurza, and J. W. Kolar, "Control and protection of a synergetically controlled two-stage boost-buck PFC rectifier system under irregular grid conditions," in *Proc. 9th Int. Power Electron. Motion Control Conf.*, 2020, pp. 1–11.
- [29] A. M. Hava, R. J. Kerkman, and T. A. Lipo, "Simple analytical and graphical methods for carrier-based PWM-VSI drives," *IEEE Trans. Power Electron.*, vol. 14, no. 1, pp. 49–61, Jan. 1999.
- [30] D.-W. Chung and S.-K. Sul, "Minimum-loss strategy for three-phase PWM rectifier," *IEEE Trans. Ind. Electron.*, vol. 46, no. 3, pp. 517–526, Jun. 1999.
- [31] T. D. Nguyen, J. Hobraiche, N. Patin, G. Friedrich, and J. P. Vilain, "A direct digital technique implementation of general discontinuous pulse width modulation strategy," *IEEE Trans. Ind. Electron.*, vol. 58, no. 9, pp. 4445–4454, Sep. 2011.
- [32] J. Xu, J. Han, Y. Wang, S. Habib, and H. Tang, "A novel scalar PWM method to reduce leakage current in three-phase two-level transformerless grid-connected VSIs," *IEEE Trans. Ind. Electron.*, vol. 67, no. 5, pp. 3788–3797, May 2020.
- [33] J. A. Anderson, M. Haider, D. Bortis, J. W. Kolar, M. Kasper, and G. Deboy, "New synergetic control of a 20kw isolated vienna rectifier front-end EV battery charger," in *Proc. 20th Workshop Control Model. Power Electron.*, 2019, pp. 1–8.
- [34] Y. Li, J. Schfer, D. Bortis, J. W. Kolar, and G. Deboy, "Optimal synergetic control of a three-phase two-stage ultra-wide output voltage range EV battery charger employing a novel hybrid quantum series resonant DC/DC converter," in *Proc. IEEE 21st Workshop Control Model. Power Electron.*, 2020, pp. 1–11.
- [35] J. W. Kolar and S. D. Round, "Analytical calculation of the RMS current stress on the DC-link capacitor of voltage-PWM converter systems," *Inst. Elect. Eng. Proc. Electr. Power Appl.*, vol. 153, no. 4, pp. 535–543, 2006.
- [36] J. Xu, T. B. Soeiro, F. Gao, H. Tang, and P. Bauer, "Minimum switching losses discontinuous PWM strategy for bidirectional single-phase AC-DC converter with active power decoupling circuit," *IEEE Trans. Power Electron.*, vol. 36, no. 5, pp. 6118–6132, May 2021.

- [37] A. M. Hava, R. J. Kerkman, and T. A. Lipo, "A high-performance generalized discontinuous PWM algorithm," *IEEE Trans. Ind. Appl.*, vol. 34, no. 5, pp. 1059–1071, Sep. 1998.
- [38] C. Hou, C. Shih, P. Cheng, and A. M. Hava, "Common-mode voltage reduction pulsewidth modulation techniques for three-phase grid-connected converters," *IEEE Trans. Power Electron.*, vol. 28, no. 4, pp. 1971–1979, Apr. 2013.
- [39] *Datasheet of C3M0120090J, CREE Power Applications*, Durham, NC, USA, Jan. 2018. [Online]. Available: <https://www.wolfspeed.com/media/downloads/834/C3M0120090.J.pdf>
- [40] G. Grandi, J. Loncarski, and O. Dordevic, "Analysis and comparison of peak-to-peak current ripple in two-level and multilevel PWM inverters," *IEEE Trans. Ind. Electron.*, vol. 62, no. 5, pp. 2721–2730, May 2015.
- [41] K. Jalili and S. Bernet, "Design of LCL filters of active-front-end two-level voltage-source converters," *IEEE Trans. Ind. Electron.*, vol. 56, no. 5, pp. 1674–1689, May 2009.
- [42] J. Steinke, "Use of an LC filter to achieve a motor-friendly performance of the PWM voltage source inverter," *IEEE Trans. Energy Convers.*, vol. 14, no. 3, pp. 649–654, Sep. 1999.



**Junzhong Xu** (Member, IEEE) was born in Ningbo, China, in 1994. He received the B.S. degree from the Harbin Institute of Technology, Harbin, China, in 2016, and the Ph.D. degree from Shanghai Jiao Tong University, Shanghai, China, in 2021, both in electrical engineering.

From January 2020 to June 2021, he was a Visiting Scholar with DC Systems, Energy Conversion and Storage Group, Delft University of Technology, Delft, The Netherlands. He is currently a Postdoctoral Research Fellow with the Department of Electrical

Engineering, Shanghai Jiao Tong University. His research interests include advanced control and modulation for power converters.



**Thiago Batista Soeiro** (Senior Member, IEEE) received the B.S.(Hons.) and M.S. degrees in electrical engineering from the Federal University of Santa Catarina, Florianopolis, Brazil, in 2004 and 2007, respectively, and the Ph.D. degree from the Swiss Federal Institute of Technology, Zurich, Switzerland, in 2012.

During the master's and Ph.D. studies, he was a Visiting Scholar with Power Electronics and Energy Research Group, Concordia University, Montreal, QC, Canada, and with the Center for Power Electronics

Systems, Blacksburg, VA, USA. From 2012 to 2013, he was a Senior Engineer with Power Electronics Institute, Federal University of Santa Catarina. From 2013 to 2018, he was a Senior Scientist with Corporate Research Center, ABB Switzerland Ltd., Baden, Switzerland. Since 2018, he has been with DC Systems, Energy Conversion and Storage Group, Delft University of Technology, Delft, The Netherlands, where he is currently an Associate Professor of high-power electronics. In January 2022, he will join the European Space Research and Technology Centre, European Space Agency, Noordwijk, The Netherlands, where he will work on the R&D of power conditioning and distribution units for satellites.



**Yang Wu** (Student Member, IEEE) received the B.S. degree in electrical engineering and automation from Southeast University, Nanjing, China, in 2017, and the M.Sc. (*cum laude*) degree in electrical power engineering in 2019 from the Delft University of Technology, Delft, The Netherlands, where he is currently working toward the Ph.D. degree in electrical engineering with DC Systems, Energy Conversion and Storage Group.



**Fei Gao** (Member, IEEE) received the Ph.D. degree in electrical engineering from Power Electronics, Machines, and Control Research Group, University of Nottingham, Nottingham, U.K., in 2016.

From March 2010 to September 2012, he was with Jiangsu Electric Power Research Institute, State Grid Corporation of China, Nanjing, China. From 2016 to 2019, he was a Postdoctoral Researcher with the Department of Engineering Science, University of Oxford, Oxford, U.K. Since July 2019, he has been an Associate Professor with Shanghai Jiao Tong University, Shanghai, China. His current research interests include modeling, control, power management and stability of microgrids, and more electric transportation systems.

Dr. Gao is the recipient of the European Union Clean Sky Best Ph.D. Award in 2017 and the *IET Control and Automation* Runner Up Ph.D. Award in 2018.



**Yong Wang** (Member, IEEE) received the Ph.D. degree in power electronics from Zhejiang University, Hangzhou, China, in 2005.

From 2005 to 2008, he was a Senior Researcher with the Samsung Advanced Institute of Technology, Suwon, South Korea, working on the fuel cell grid-tied inverter. From 2008 to 2010, he was a Power Electronics Hardware Engineer with Danfoss Solar Inverters, Soenderborg, Denmark. In 2010, he joined Shanghai Jiao Tong University, Shanghai, China, where he is currently a Full Professor with the Department of Electrical Engineering. His main research interests include grid-tied inverter technology, high-frequency dc–dc converter based on wide-bandgap devices applied in electric vehicle, and wireless power transfer.

Dr. Wang is the recipient of the European Union Clean Sky Best Ph.D. Award in 2017 and the *IET Control and Automation* Runner Up Ph.D. Award in 2018.



**Houjun Tang** received the Ph.D. degree in automation from Yamagata University, Yamagata, Japan, in 1997.

He is currently a Full Professor with the Department of Electrical Engineering, Shanghai Jiao Tong University, Shanghai, China. His research interests include wireless power transform, motor drive inverters, and power converters.



**Pavol Bauer** (Senior Member, IEEE) received the master's degree in electrical engineering from the Technical University of Kosice, Košice, Slovakia, in 1985, and the Ph.D. degree from the Delft University of Technology, Delft, The Netherlands, in 1995.

He is currently a Full Professor with the Department of Electrical Sustainable Energy, Delft University of Technology, where he is also the Head of DC Systems, Energy Conversion and Storage Group. He has authored or coauthored more than 72 journal papers and almost 300 conference papers in his field

(with H factor Google scholar 43, and Web of science 20). He is also an author or coauthor of eight books. He holds four international patents and organized several tutorials at the international conferences. He has worked on many projects for industry concerning wind and wave energy, power electronic applications for power systems such as Smarttrafo; HVDC systems; and projects for smart cities such as photovoltaic (PV) charging of electric vehicles, PV and storage integration, and contactless charging. He participated in several Leonardo da Vinci and H2020 EU projects as a project partner (ELINA, INETELE, and E-Pragmatic) and a coordinator (PEMCWebLab.com-Edipe, SustEner, and Eranet DCMICRO).

Dr. Bauer was a recipient of the Title of Professor from the President of Czech Republic at the Brno University of Technology in 2008 and at the Delft University of Technology in 2016.